

UCSF

UC San Francisco Electronic Theses and Dissertations

Title

Early Life Inflammation Primes a Th2-Fibroblast Niche in Skin

Permalink

<https://escholarship.org/uc/item/7dp1k6wb>

Author

Boothby, Ian Chen

Publication Date

2021

Peer reviewed|Thesis/dissertation

Early Life Inflammation Primes a Th2-Fibroblast Niche in Skin

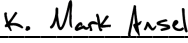
by
Ian Boothby

DISSERTATION
Submitted in partial satisfaction of the requirements for degree of
DOCTOR OF PHILOSOPHY

in
Biomedical Sciences

in the
GRADUATE DIVISION
of the
UNIVERSITY OF CALIFORNIA, SAN FRANCISCO

Approved:


DocuSigned by:

BC645044B450408... K. Mark Ansel
Chair

DocuSigned by:

BC645044B450408... Jason Cyster

DocuSigned by:

BC645044B450408... Tien Peng

DocuSigned by:

B9C7E7603EE44D5... Michael Rosenblum

Committee Members

Dedicated to my parents, Jin Chen and Mark Robin Boothby, and my grandparents William M.
Boothby, Ruth Boothby, and Chaxian Wang.

ACKNOWLEDGEMENTS

An important theme in biology that has been pivotal to my thesis work is that no cell, organism, or species can grow or develop without an environment that nurtures and supports it. In some contexts this is called an “instructive niche”; more generally, we can think of this simply as a community. Likewise, my graduate education is the product of a community that has given me immense support, opportunity, satisfaction, and joy in the past four and a half years. There are too many people who have helped chart the course of my PhD to acknowledge in their entirety here, but I’d like to give special thanks to a few people in particular below.

My thesis advisor, Dr. Michael Rosenblum, has given me terrific mentorship and trained me from a student to a scientist. He has given me tremendous independence and resources to pursue exciting science, and has always imparted in me his enthusiasm and passion for research and a keen focus on attacking the big questions. I’d also like to thank my high school and undergraduate mentors, Drs. David Miller and Jeff Lichtman, who took chances on me as a raw and untrained student and supported me in my journey to the next stages of training. To Drs. Ari Molofsky, Tiffany Scharschmidt, and Cliff Lowell, I am extremely grateful for the many hours spent hearing and critiquing my work at our 12th floor joint lab meeting, and for the uniquely collegial environment that they have established in HSW-12. Along with Mike, these are the professors that I look to as model physician-scientists, colleagues, mentors, and leaders. I also would like to give special thanks to my thesis committee members, Drs. Mark Ansel, Tien Peng, Jason Cyster, as well as my MSTP advisor Dr. Averil Ma, all of whom have provided me with excellent advice on my project, graciously read over drafts of papers and grants, and provided me with invaluable career guidance.

Within the Rosenblum lab, I would first and foremost like to thank Margaret Lowe, who trained me as a rotation student and has continued to be a source of advice, support, and shenanigans. I was lucky to have Joshua Moreau as my bench-mate, whose rigor and plain-spoken scientific common sense were a tremendous influence on me; as well as Dr. Jarish Cohen nearby, who taught me nearly everything I know about pathology and is a never-ending source of experimental creativity and great discussions about research. I've been privileged to work with many other fantastic scientists and friends who joined the Rosenblum lab and neighboring labs on the floor—Anu, Pooja, the Kellys, Lucky, Irek, Vic, Tim, Bahar, Candice, Madison, Geil, Jeanmarie, John, Antonin, Miqdad, Madelene, Stephen, Nick Mroz, Kelly Cautivo, Marcela, Catherine, Julia, Nathan, Nick Rutsche, Wes, Otto, Su-Yang, and Clare (hope I'm not leaving anyone out here!). And of course, none of this would be possible without Mariela Pauli, who (along with Maggie) is the hub that keeps the research, culture, and spirit of the lab spinning.

I'd like to give particular thanks to the colleagues who helped me turn scientific ideas into results. Devi Boda, Courtney Macon, and Elaine Kwan worked long hours with me on many experiments and have been great mentees and friends. Maxime Kinet has been a wonderful mentor as a physician-scientist and co-conspirator in research, and I'm excited to see where he takes our projects next. I've been lucky to work with so many experienced scientists at various UCSF core facilities, including Ashley and Vinh at the Flow Core; Carine, Anthony, and Climena at IACUC/LARC; Kyle, Jordan, John, and Taylor at BIDC; Annie and Cat at the Genomics CoLab, and many others.

Throughout my training, I've always felt at home in the BMS and MSTP programs at UCSF. The directors and administrators of these programs—Mark Anderson, Aimee Kao, Catherine Lomen-Hoerth, Amanda Andonian, Andres Zepeda, Demian Sainz, Ned Molyneaux,

Anita Sil, and Mark Ansel—have made my time in the PhD years as seamless as possible, and I can think of many occasions when conversations and advice from these people got me through a bump in my training. A special thank-you must be reserved for Geri Ehle, the chief administrator of the MSTP program and perhaps most beloved figure in the MSTP community (certainly by me!) I wish I had space to acknowledge all of the incredible friends and peers I've met, but I'll mention a few who have given me especially meaningful help and camaraderie in my professional life: Theo Roth, David Wu, Lay Kodama, Parinaz Fozouni, Stacey Frumm, Jinwoo Lee, Antonia Gallman, Devan Diwanji, and Karsyn Bailey. My MSTP class has been some of my closest friends, and I'll always cherish memories of our trips to Spain and San Diego and the annual Christmas parties. To my MSTP roommates past and present—Paul Wei, Kun Leng, Marissa Chou, and Ricky Guajardo—I couldn't imagine a more supportive or inspiring group of people to live with. I hope we'll still be cooking, complaining, and laughing together for many years to come. Eric and Sarah—I hope you'll be there too! My friends outside UCSF have also made life joyful even when things were at their hardest: Josh, Sam, Maya, Angie, Raina, Faith, Sherrie, Stephen, Olu, David Kersen, Danny, Jamie, and Diana.

Finally comes my family, to whom I owe all the most important accomplishments in my life. My grandparents, especially my grandmother 王茶仙, started with nothing and gave me everything. My uncle Daniel and cousins Rose, Clara, Gregg, Jason, and Xiaoqian (along with niece Mira) have all been a beloved part of my life in these years. My partner Lakshmi has been my best friend, closest confidante, clinical role model, and the spark for my fire, both in lab and outside. Mom and Dad, I'm not sure if you imagined my seedling growing so close to the oak trees when you let 3-year old Ian play with the pipettes in your lab. But here we are, and I'll always cherish the even-handed guidance and unqualified love you've given me.

CONTRIBUTIONS TO PRESENTED WORK

The majority of the work presented in chapter 2 of this thesis is published as **Boothby IC***, Kinet MJ, Boda DP...Rosenblum MD. Early Life Inflammation Primes a T Helper 2 Cell-Fibroblast Niche in Skin, *Nature* (2021), with Ian Boothby as first author. It has been reproduced here in accordance with the policies of Nature Publishing Group. This work was done with the supervision, guidance, and funding of Dr. Michael Rosenblum. I.C.B. and M.D.R. conceptualized the project, and experimental design and data analysis were performed by I.C.B. Experiments were carried out by I.C.B. with assistance from M.J.K., D.P.B., S.C., E.K., I.H., and J.C. Human sample procurement was coordinated by M.M.L., M.P., A.E.Y., J.D.C., H.W.H., I.M.N., T.H.M., and M.D.R. Writing was done by I.C.B., with editing input from A.B.M. and M.D.R.

ABSTRACT

Early Life Inflammation Primes a T Helper 2 Cell-Fibroblast Niche in Skin

Ian Chen Boothby

Inflammation early in life can prime the local immune milieu of peripheral tissues, causing lasting changes in immunologic tone that confer disease protection or susceptibility. The cellular and molecular mechanisms that incite changes in immune tone in many nonlymphoid tissues remain largely unknown. We find that time-limited neonatal inflammation induced by transient reduction of neonatal regulatory T cells (Tregs) causes a dramatic dysregulation of subcutaneous tissue in murine skin, accompanied by the selective accumulation of Th2 cells within a distinct microanatomic niche. Th2 cells are maintained into adulthood through interactions with a fibroblast population in skin fascia that we refer to as Th2-interacting fascial fibroblasts (TIFFs), which expand in response to Th2 cytokines to form subcutaneous fibrous bands. Activation of the Th2-TIFF niche by neonatal inflammation primes skin for altered reparative responses to wounding. We further identify fibroblasts in healthy human skin expressing the TIFF transcriptional signature and find these cells at high levels in eosinophilic fasciitis, an orphan disease characterized by inflammation and fibrosis of the skin fascia. Taken together, these data define a novel Th2 niche in skin, functionally characterize a disease-associated fibroblast population, and suggest a mechanism of immunologic priming whereby inflammation early in life creates networks between adaptive immune cells and stromal cells, establishing an immunological set-point in tissues that is maintained throughout life.

TABLE OF CONTENTS

<i>Chapter 1: Introduction</i>	<u>1</u>
References	<u>4</u>
<i>Chapter 2: Early Life Inflammation Primes a Th2-Fibroblast Niche in Skin</i>	<u>7</u>
References	<u>50</u>

LIST OF FIGURES

Figure 2.1	Transient neonatal Treg reduction causes temporary derangement of stromal architecture and lasting Th2 accumulation in the skin subcutis.	32
Figure 2.2	NeoTreg reduction causes outgrowth of an <i>Il13ra1</i> ⁺ fibroblast population in skin fascia.	33
Figure 2.3	Figure 2.3- Reciprocal interactions between skin Th2 Cells and <i>Il13ra1</i> ⁺ fibroblasts (TIFFs) drive fascial expansion and Th2 maintenance	34
Figure 2.4	Figure 2.4- TIFF-like cells are present in healthy human skin and in a fibroinflammatory disease of the fascia.	35
Figure S2.1	Characteristics of cutaneous inflammation induced by neonatal Treg reduction.	36
Figure S2.2	Resolution of inflammation and return to homeostasis following neonatal Treg reduction.	38
Figure S2.3	CD49d marks subcutis-resident Th2 cells that are associated with subdermal eosinophilia and age-specific fibrous band formation.	39
Figure S2.4	Single-cell transcriptomic characterization of skin stroma in control and Δ neoTreg mice.	40
Figure S2.5	<i>Il13ra1</i> ⁺ FBs / TIFFs are transcriptomically similar to <i>Pil6</i> ⁺ fibroblasts found across mouse organs.	42
Figure S2.6	Anatomic characterization of <i>Il13ra1</i> ⁺ fibroblasts (TIFFs)	44

Figure S2.7	Further characterization of Th2-TIFF interactions in the subdermal niche.	45
Figure S2.8	Th2-TIFF interactions and niche priming across multiple models of early life subcutaneous inflammation.	46
Figure S2.9	Figure S2.9- Neonatal Treg reduction primes skin for Th2-driven tissue reparative responses during adulthood.	47
Figure S2.10	Characterization of human skin stroma.	49

Chapter 1: Introduction

Epidemiologic evidence suggests that infancy and childhood constitute a critical window in the development of the immune system that can alter immune responses during adulthood^{1,2}. Barrier organs such as the skin, respiratory tract, and gastrointestinal tract undergo substantial changes in immune cell composition between birth and adulthood and are primary sites of antigen exposure and inflammation during this time³⁻⁵. The adult immune compartments of these tissues are first seeded by developmentally pre-programmed waves of immune cell migration in the perinatal time period consisting primarily of innate cells^{4,6}. Tissue immune compartments are subsequently remodeled during postnatal and adult life by extrinsic stimuli such as infection⁷, commensal microbial colonization⁸⁻¹⁰ and autoimmune or allergic inflammation¹¹, resulting in the addition of adaptive immune cell types such as tissue resident-memory T cells (T_{RM}) to the pool of tissue-resident cells. Both innate and adaptive tissue-resident lymphocytes are maintained within specialized microanatomic niches composed of parenchymal cell types that produce factors necessary for lymphocyte survival and/or activation¹²⁻¹⁴. The layered population of tissue niches throughout postnatal development has been proposed as a mechanism of tissue imprinting—that is, inflammation during early life may permanently alter the immunologic tone of peripheral (*i.e.*, non-lymphoid) tissues by inducing the residency of novel tissue-resident immune cell types^{15,16}. However, it is currently unclear how this phenomenon may occur.

Regulatory T cells (Tregs) play an integral role in maintaining immune homeostasis and suppressing inflammation throughout life¹⁷. Tregs generated in the neonatal period are phenotypically and functionally distinct from adult Tregs, and the presence of these cells early in life is required for the establishment of tolerance to commensal microbes and prevention of pathologic imprinting during adulthood¹⁸⁻²⁰. Qualitative and/or quantitative defects in Tregs

have been linked to the development of human autoimmune and allergic diseases, and retrospective analysis of childhood atopy suggest that microbial and environmental influences can affect the risk of developing disease later in life by altering the neonatal Treg compartment^{21,22}. While major Treg deficiencies are capable of unleashing multiple arms of effector immunity, some peripheral tissues have a propensity to develop polarized inflammatory responses. For instance, Treg impairment causes Th17-biased inflammation in the colon, whereas human and murine mutations in the Treg-defining transcription factor FoxP3 lead to Th2-polarized responses in skin and severe eczematous dermatitis from a young age^{23–25}. Here, we focus on skin, a quintessential barrier tissue in which Tregs are highly abundant during postnatal development¹⁹. We induce time-limited cutaneous inflammation early in life by reducing neonatal Tregs and find that this temporarily induces a dramatic dysregulation of skin stromal architecture, followed by the selective accumulation and long-term persistence of Th2 cells (but not other lymphocytes) into adulthood. Skin Th2 cells reside in a unique niche in the subcutis and interact with a stromal cell type that we term “Th2-interacting fascial fibroblasts” (TIFFs), which produce IL-33 and expand in response to Th2 cytokine production. The formation of this niche not only enables Th2 accumulation and persistence in skin but also alters the immunologic tone of adult skin by changing the reparative response of the cutaneous myeloid and stromal compartments during wound healing. We thus propose that the population of lymphocyte niches may constitute one mechanism by which immunologic events early in life can change the immunologic setpoint of tissues, influencing inflammatory responses and disease susceptibility throughout adulthood.

References

1. Lambrecht, B. N. & Hammad, H. The immunology of the allergy epidemic and the hygiene hypothesis. *Nat. Immunol.* **18**, 1076–1083 (2017).
2. Hornef, M. W. & Torow, N. ‘Layered immunity’ and the ‘neonatal window of opportunity’ – timed succession of non-redundant phases to establish mucosal host–microbial homeostasis after birth. *Immunology* **159**, 15–25 (2020).
3. Thome, J. J. C. *et al.* Early-life compartmentalization of human T cell differentiation and regulatory function in mucosal and lymphoid tissues. *Nat. Med.* **22**, 72–77 (2016).
4. de Kleer, I. M. *et al.* Perinatal Activation of the Interleukin-33 Pathway Promotes Type 2 Immunity in the Developing Lung. *Immunity* **45**, 1285–1298 (2016).
5. Gollwitzer, E. S. *et al.* Lung microbiota promotes tolerance to allergens in neonates via PD-L1. *Nat Med* **20**, 642–7 (2014).
6. Ginhoux, F. & Guilliams, M. Tissue-Resident Macrophage Ontogeny and Homeostasis. *Immunity* **44**, 439–449 (2016).
7. Zaid, A. *et al.* Persistence of skin-resident memory T cells within an epidermal niche. *Proc. Natl. Acad. Sci. U. S. A.* **111**, 5307–5312 (2014).
8. Linehan, J. L. *et al.* Non-classical Immunity Controls Microbiota Impact on Skin Immunity and Tissue Repair. *Cell* **172**, 784-796.e18 (2018).
9. Mao, K. *et al.* Innate and adaptive lymphocytes sequentially shape the gut microbiota and lipid metabolism. *Nature* **554**, 255–259 (2018).
10. Constantinides, M. G. *et al.* MAIT cells are imprinted by the microbiota in early life and promote tissue repair. *Science (80-.).* **366**, (2019).
11. Clark, R. A. Resident memory T cells in human health and disease. *Science Translational*

- Medicine* (2015) doi:10.1126/scitranslmed.3010641.
12. Adachi, T. *et al.* Hair follicle-derived IL-7 and IL-15 mediate skin-resident memory T cell homeostasis and lymphoma. *Nat. Med.* **21**, 1272–1279 (2015).
 13. Dahlgren, M. W. *et al.* Adventitial Stromal Cells Define Group 2 Innate Lymphoid Cell Tissue Niches. *Immunity* **50**, 1–16 (2019).
 14. Spallanzani, R. G. *et al.* Distinct immunocyte-promoting and adipocyte-generating stromal components coordinate adipose tissue immune and metabolic tenors. *Sci. Immunol.* **4**, 1–14 (2019).
 15. Kotas, M. E. & Locksley, R. M. Why Innate Lymphoid Cells? *Immunity* **48**, 1081–1090 (2018).
 16. Al Nabhani, Z. & Eberl, G. Imprinting of the immune system by the microbiota early in life. *Mucosal Immunol.* **13**, 183–189 (2020).
 17. Josefowicz, S. Z., Lu, L.-F. & Rudensky, A. Y. Regulatory T Cells: Mechanisms of Differentiation and Function. *Annu. Rev. Immunol.* **30**, 531–64 (2012).
 18. Yang, S., Fujikado, N., Kolodin, D., Benoist, C. & Mathis, D. Regulatory T cells generated early in life play a distinct role in maintaining self-tolerance. *Science* (80-.). **348**, 589–594 (2015).
 19. Scharschmidt, T. C. *et al.* A Wave of Regulatory T Cells into Neonatal Skin Mediates Tolerance to Commensal Microbes. *Immunity* **43**, 1011–1021 (2015).
 20. Nabhani, Z. Al *et al.* A Weaning Reaction to Microbiota Is Required for Resistance to Immunopathologies in the Adult Article A Weaning Reaction to Microbiota Is Required for Resistance to Immunopathologies in the Adult. *Immunity* **50**, 1–13 (2019).
 21. Fujimura, K. E. *et al.* Neonatal gut microbiota associates with childhood multisensitized

- atopy and T cell differentiation. *Nat Med* **22**, (2016).
22. Levan, S. R. *et al.* Elevated faecal 12,13-diHOME concentration in neonates at high risk for asthma is produced by gut bacteria and impedes immune tolerance. *Nat. Microbiol.* **4**, 1851–1861 (2019).
 23. Wildin, R. S. *et al.* X-linked neonatal diabetes mellitus, enteropathy and endocrinopathy syndrome is the human equivalent of mouse scurfy. *Nat. Genet.* **27**, 18–20 (2001).
 24. Halabi-Tawil, M. *et al.* Cutaneous manifestations of immune dysregulation, polyendocrinopathy, enteropathy, X-linked (IPEX) syndrome. *Br. J. Dermatol.* **160**, 645–51 (2009).
 25. Chaudhry, A. *et al.* CD4⁺ regulatory T cells control Th17 responses in a Stat3-dependent manner. *Science (80-.).* **326**, 986–991 (2009).

Chapter 2: Early Life Inflammation Primes a Th2-Fibroblast Niche in Skin

Published previously as:

Ian C. Boothby, Maxime J. Kinet, Devi P. Boda, Elaine Y. Kwan, Sean Clancy, Jarish N. Cohen,
Ireneusz Habrylo, Margaret M. Lowe, Mariela Pauli, Ashley E. Yates, Jamie D. Chan, Hobart
W. Harris, Isaac M. Neuhaus, Timothy H. McCalmont, Ari B. Molofsky, and Michael D.
Rosenblum

Early Life Inflammation Primes a T Helper 2-Cell Fibroblast Niche in Skin. *Nature*, 2021. DOI:
10.1038/s41586-021-04044-7.

Main Text

Inflammation early in life can prime the local immune milieu of peripheral tissues, causing lasting changes in immunologic tone that confer disease protection or susceptibility.¹ The cellular and molecular mechanisms that incite changes in immune tone in many nonlymphoid tissues remain largely unknown. A wave of neonatal Tregs (neoTregs) seeds murine skin between postnatal days 6 and 13 (P6 - P13)^{2,3}. We hypothesized that attenuating this Treg wave could influence postnatal development of the skin immune compartment and tested this by administering two injections of low-dose diphtheria toxin (DT) to *FoxP3^{DTR}* mice⁴ at postnatal days 8 and 15 (P8 and P15). Unlike continuous dosing, which causes uncontrolled autoimmunity⁴, two-shot dosing caused transient T cell-mediated inflammation with minimal weight loss or gross clinical symptoms of autoimmunity and full restoration of the cutaneous and lymphoid Treg compartments (**Fig. S2.1a-f**).

The epidermis and dermis of skin sit atop layers of adipocytes and stroma called the subcutis or hypodermis (**Fig. 2.1a**). During the inflammatory phase after neoTreg reduction, we observed a striking architectural derangement of the subcutis characterized by adipocyte loss and formation of hyperplastic fibrous bands (**Fig. 2.1b-c**). Qualitative stromal expansion was also present in gonadal adipose tissue but not in ear skin, lung, or colon, whereas fibrous bands were not present in DT-injected wildtype mice (**Fig. S2.1g-h**). Δ Treg adults experienced a comparable loss of Tregs and immune infiltration; however, adipocytes were intact and fibrous bands were not observed (**Fig. 2.1d, Fig. S2.1c-f**). Thus, transient Treg reduction causes age-specific subcutaneous dysfunction and expansion of an unknown stromal cell type.

Durable Accumulation of Th2 Cells in the Skin Subcutis After Neonatal Inflammation

We next investigated whether Δ neoTreg mice had lasting alterations in skin. Skin architecture normalized over time and the immune composition of Δ neoTreg skin resembled controls by adulthood, with one exception: an increase in skin Th2 cells (**Fig. 2.1e-h, Extended Data 2a-f**). Using an *Il5^{Red5}* reporter to more accurately identify Th2 cells,⁵ we determined that Th2 cells were absent in skin of control adults but comprised ~8-12% of CD4⁺ T effector cells (Teffs) in Δ neoTreg adult skin and persisted at least 90 days post-DT (**Fig. 2.1f-g**). Th2 cells were selectively increased in skin, with no corresponding elevations in other major cutaneous lymphocyte subsets (**Fig. 2.1h, Fig. S2.2d-f**).

Skin lymphocytes in naïve mouse skin reside primarily in the epidermis and dermis and express the integrin CD103⁶⁻⁸. By contrast, skin Th2 cells in Δ neoTreg mice were CD103⁻ and instead expressed CD49d (α_4 integrin; **Fig. 2.1i, Fig. S2.3a-c**). Using confocal microscopy and flow cytometry of separated skin layers, we found that lymphocytes' integrin expression correlated with their microanatomic localization, with CD49d⁺ Th2 cells located preferentially in the subcutis and other skin lymphocytes found in the dermis and epidermis (**Fig. 2.1j-k, Fig. S2.3d-e**). The minority of non-Th2 lymphocytes found in the subcutis were also predominantly CD49d⁺ (**Fig. S2.3f**). The CD49d⁺ CD103⁻ phenotype may thus be a shared feature of lymphocytes in this region of skin.

Since CD49d⁺ Th2 cells and fibrous bands both appeared in the subcutis, we investigated whether differential Th2 responses in neonates and adults correlated with the age-specific formation of fibrous bands. More CD49d⁺ Th2 cells and eosinophils accumulated in Δ neoTreg mice than Δ adTreg mice at the time of fibrous band formation (**Fig. S2.3g-i**). Treatment of Δ neoTreg mice with the lymph node egress inhibitor FTY720 attenuated skin Th2 accumulation

as well as fibrous band formation (**Fig. S2.3j-l**). However, by 35 days post-injection, CD49d⁺ Th2 cells were present at similar frequencies in both Δ neoTreg and Δ adTreg mice (**Fig. S2.3m-n**), suggesting that the lower number of Th2 cells that seed the adult subcutis during inflammation persist in this region of skin after inflammation resolves. Therefore, although the greater magnitude of type 2 inflammation in Δ neoTreg mice correlates with fibrous band formation, the subcutis can support Th2 cells without requiring fibrous band formation to license their residency.

An *Il13ra1*⁺ Fascial Fibroblast Population Accumulates After NeoTreg Reduction

The co-occurrence of Th2 accumulation and fibrous band formation in Δ neoTreg mice prompted us to seek stromal population(s) present in the fibrous bands that might interact with type 2 immune cells. Single-cell RNA sequencing (scRNAseq) of stromal cells (CD45⁻ EpCAM⁻ CD31⁻) sorted from control and Δ neoTreg skin revealed two clusters that are highly elevated in Δ neoTreg skin and preferentially express the Th2 cytokine receptor genes *Il4ra* and *Il13ra1* (**Fig. 2.2a-c**). These two clusters were likely the same cell type, with the smaller cluster undergoing proliferation (**Extended Data 4a**). *Il13ra1*⁺ stromal cells expressed canonical fibroblast markers, extracellular matrix (ECM) components, and numerous immune-related genes, and neoTreg reduction led these cells to upregulate ECM components such as *Fnl1* and *Postn* and the eosinophil chemoattractant *Ccl11* (**Fig. S2.4b-e**). Comparison to a recent cross-tissue meta-analysis of murine fibroblasts demonstrated that *Il13ra1*⁺ fibroblasts bear a strong transcriptional similarity to a *Pil6*⁺ *Anxa3*⁺ fibroblast subset present in many organs (**Extended Fig. 5**).⁹ Although these cells have been annotated in recent single-cell atlases,^{10,11} a unified understanding of their phenotypic, anatomic, and functional characteristics remains to be elucidated.

Guided by transcriptional data, we validated a flow cytometry gating strategy for skin *Il13ral*⁺ FBs as Lin⁻ CD34⁺ PDPN⁺ Sca1⁺ CD26⁺ CD9⁻ (**Fig. 2.2d-f; Fig. S2.4f-g**).

Immunofluorescence (IF) microscopy revealed high-intensity CD26 staining in the fascia, the lowermost layer of the subcutis in mice (**Fig. 2.1a, 2g**). CD26^{hi} fascia was present in back skin but not ear or tail skin and was generally located beneath the panniculus carnosus (PC) skeletal muscle layer, although it could also be found adjacent to adipocytes in regions lacking PC (**Fig. S2.6a-b**). Although papillary dermal fibroblasts also express CD26 at lower levels¹² (**Fig. 2g**), *Il13ral*⁺ FBs could be found only in the subcutis upon flow cytometry of separated skin layers, consistent with fascial localization (**Fig. S2.6c**). We additionally used scRNAseq to identify *Fgf18* as a marker of *Il13ral*⁺ FBs and verified their localization in *Fgf18*^{CreERT2}; *Rosa26*^{tdTomato} mice. Stellate CD26⁺ FGF18⁺ cells were primarily located in the fascia, with sparser FGF18⁺ cells higher in the subcutis (**Fig. S2.6d-e**). As expected, FGF18⁺ hair follicle keratinocytes not captured in our scRNAseq dataset were also present.¹³ Given the pronounced expansion of CD26^{hi} fascia (by IF) and increased *Il13ral*⁺ FBs (by flow cytometry) after neoTreg depletion, we conclude that fibrous bands in Δ neoTreg mice derive from the expansion of fascial *Il13ral*⁺ FBs (**Fig. 2.2g-h**) and provisionally refer to these cells as Th2-interacting fascial fibroblasts (TIFFs).

Reciprocal Th2-TIFF Interactions Drive Fascial Expansion and Th2 Maintenance

TIFF expression of *Il13ral*⁺ suggested that these cells may respond to Th2 cytokines. Subcutaneous injection of either the Th2 effector cytokines IL-4 and IL-13 or the Th2-inducing alarmin IL-33 spurred TIFF proliferation and fascial expansion in young wildtype mice, histologically resembling the fibrous bands seen after neoTreg reduction (**Fig. 2.3a-b, Fig.**

S2.7a). Conversely, TIFF expansion was attenuated in Δ neoTreg mice crossed to either *Il4/Il13* or *Il33*-deficient strains (**Fig. 2.3c-d, Fig. S2.7b**). Interestingly, TIFFs expressed lower levels of IL4RA in adult mice than in young mice (**Fig. S2.7c**). In contrast to adTreg reduction, exogenous cytokine delivery drove fascial expansion in adult mice accompanied by increases in skin ILC2s and eosinophils, suggesting that supraphysiologic type 2 immune stimuli can expand TIFFs regardless of age. (**Fig. S2.7d-f**). To test whether TIFFs enhance skin Th2 cell survival and/or activation, we next isolated skin IL5^{Red5+} Th2 cells from Δ neoTreg mice and co-cultured them with primary TIFFs or dermal FBs. Co-culture with TIFFs facilitated higher Th2 cell numbers, proliferation, and IL-5 production than dermal FBs (**Fig. 2.3e-f, Fig. S2.7g-h**). These data suggest that Th2 cells preferentially maintained within the subcutis after neonatal inflammation may receive support from TIFFs that promotes their survival, proliferation, and/or activation.

Activation of type 2 immune responses in skin is initiated in part by local release of alarmins such as TSLP, IL-18, and IL-33¹⁴⁻¹⁶. We found that ~80% of skin Th2 cells in Δ neoTreg mice expressed the IL-33 receptor ST2, in contrast to other skin-resident lymphocyte populations, which were largely ST2⁻ IL-18R1⁺ (**Fig. 2.3g, Fig. S2.7i-j**). Similar to the expression pattern of integrins CD103 and CD49d, lymphocyte IL-18R1 and ST2 corresponded to tissue localization, with ST2 enriched in subdermal lymphocytes and IL-18R1 found in epidermis/dermis-resident cells (**Fig. S2.7k-l**). Polarized expression of integrins and alarmin cytokine receptors may therefore reflect a stratification of skin lymphocytes into epithelial-associated and pure-stromal niches. Using an *Il33*^{H2B-mCherry} reporter mouse line, we noted higher IL-33 production in TIFFs than other stromal populations (**Fig. 2.3h-i**). IL-33 deficient *Il33*^{mch/mch}; *FoxP3*^{DTR} mice showed reduced accumulation of skin Th2 cells following neoTreg reduction, whereas subcutaneous injection of IL-33 into adult Δ neoTreg mice robustly expanded

skin Th2 cells (**Fig. 2.3j-k**). Taken together, these data suggest that IL-33 production is one mechanism by which TIFFs support skin Th2 cells within the subdermal niche.

Multiple Models of Subcutaneous Inflammation Can Prime the Th2-TIFF Niche

Treg depletion unleashes a pleiotropic systemic immune response that may not reflect physiologic inflammation. We therefore tested whether key features of Δ neoTreg mice—durable accumulation of CD49d⁺ skin Th2s and TIFF expansion—occur in other models of inflammation. Subcutaneous immunization with ovalbumin (OVA) and papain spurred TIFF and Th2 accumulation after 7 days, with CD49d⁺ Th2 cells persisting in skin at least 30 days post-injection (**Fig. S2.8a-d**). TIFF accumulation was blunted in OVA-papain immunized mice with a fibroblast-specific deletion of *Il4ra*, mirroring Δ neoTreg mice and demonstrating that cell-intrinsic type 2 cytokine signaling is required for maximal TIFF expansion (**Fig. S2.8e-f**). We also exposed mice to the helminth *Nippostrongylus brasiliensis*, which breaches murine skin to enter circulation as part of its life cycle.¹⁷ Neonatal *N. brasiliensis* infection likewise induced TIFF and skin CD49d⁺ Th2 accumulation (**Extended Data 8g-j**). Thus, the Th2-TIFF niche can be primed by a variety of early life immune stimuli that cause type 2 inflammation in the subcutis.

Early Life Inflammation Primes Skin for Reparative Responses During Adulthood

Priming of the skin Th2-TIFF niche in Δ neoTreg mice suggested that early life inflammation might alter adult immune responses. Indeed, re-challenge of Δ neoTreg mice (but not controls) with DT during adulthood recapitulated the stromal dysfunction seen after neonatal Treg depletion (**Fig. S2.9a-b**). We next tested the immune response of Δ neoTreg skin to full-

thickness wounding, a process modulated by pro-reparative signals from type 2 immune cells that receives major contributions from subdermal fibroblasts^{12,18}. Moreover, recent work has shown that fascial tissue can migrate into wound beds, bringing along resident immune cells¹⁹. To test whether any observed differences in wound healing of Δ neoTreg mice were Th2-dependent, we also wounded Δ neoTreg/ Δ Th2 littermates (*Il5^{Red-5/+}*; *Rosa26^{DTA/+}*; *FoxP3^{DTR}*), in which skin Th2 cells are reduced by ~85% (**Fig. S2.9c**). Although both ILC2 and Th2 cells are diminished in Δ neoTreg/ Δ Th2 mice, skin ILC2 cells numbers were not increased in Δ neoTreg mice before or after wounding, making ILC2-driven differences in wound healing less likely (**Fig. S2.9c-d**).

Skin Th2 cells in Δ neoTreg mice responded robustly to wounding, quadrupling in wound beds within 4 days after injury (**Fig. S2.9e-g**). Δ neoTreg mice experienced faster wound closure (quantified by the rate constant k)²⁰ and greater accumulation of Th2-responsive myeloid populations than control or Δ neoTreg/ Δ Th2 mice (**Fig. S2.9h-k**). TIFFs were initially reduced after wounding but rebounded to a greater extent in Δ neoTreg skin during the proliferative stage of healing (**Fig. S2.9l-n**), suggesting enhanced regeneration of the fascia in these mice. These wound healing parameters were unaffected by treatment with FTY720, consistent with skin-resident Th2 cells rather than lymph node-primed Th2 cells driving repair (**Fig. S2.9o-u**). Similar effects were observed in wounded mice neonatally immunized with OVA/papain (**Fig. S2.9v-ab**). Taken together, these data indicate that early-life priming of the Th2-TIFF niche increases reparative responses during adulthood.

TIFF-like Fibroblasts are Present in Healthy Human Skin and in a Th2-Associated Fibroinflammatory Disorder of the Fascia

Numerous layers of fascia have been identified anatomically in humans, including superficial fascia in the skin subcutis.²¹ To test whether TIFFs exist in humans, we performed scRNAseq on FACS-purified stroma from three samples of healthy human skin (**Fig. 2.4a, Fig. S2.10a**). We annotated two clusters of human stromal cells as potential fascial fibroblasts (fFBs) based on their preferential expression of murine TIFF markers including *PII6*, *SFRP2*, and *OGN* (**Fig. 2.4b, Fig. S2.10b**). These markers are also expressed at lower levels in another population of mouse fibroblasts that we annotated as Thbs4+ fibroblasts (**Fig. 2.4b, Fig. S2.4a**). TIFF-expressed immunologic genes such as *IL13RA1*, *CXCL12*, and *CXCL14* were enriched in human fFB1 and fFB2 cells, although *IL18* and *IL33* were not (**Fig. S2.10c**). Since no conserved cell type-defining markers have been validated for TIFFs, we employed multiple bioinformatic approaches to compare the mTIFF transcriptome to putative human fFB clusters with greater statistical rigor. Expression of the mTIFF module score was highest in human fFB clusters, and a 144-gene mTIFF signature gene set was also significantly enriched in human fFB1s and fFB2s. (**Fig. 2.4c-d**). Additionally, human fFB1 and fFB2s co-clustered with mouse TIFFs and Thbs4+ FBs upon cross-species integration of mouse and human datasets^{22,23} (**Fig. S2.10d**). Based on these analyses, we conclude that human skin contains fibroblasts that share a core transcriptional signature with TIFFs and Thbs4+ FBs, suggesting that human fFB1 and fFB2 cells types might exhibit similar biological behaviors to TIFFs during human cutaneous inflammation.

The skin pathology that we observed in Δ neoTreg mice resembles human eosinophilic fasciitis (EF/Shulman Syndrome), an orphan connective tissue disease of unknown etiology that causes chronic, painful skin tightening and induration. Similar to Δ neoTreg skin, EF features

adipocyte loss and thickening of the fascia and interlobular septae of the subcutis (**Fig. S2.10e**). Intriguingly, proposed causes of EF include Th2 inflammation and loss of immune tolerance, as several cases of EF have been reported following checkpoint blockade cancer immunotherapy.^{24,25} We hypothesized that fFB1/fFB2 cells might constitute the major cell type(s) in the fascia of EF patients and found that fFBs were present in lesional skin from one EF donor at higher frequencies than any of the previously analyzed healthy control samples (**Fig. 2.4e-f**). Additionally, GATA3⁺ CD4⁺ T cells were increased in the subcutis of EF skin as compared to the dermis and epidermis, with large numbers of these cells located near hyperplastic fascial bands (**Fig. 2.4g-h**). These findings suggest that Δ neoTreg mice may model key features of EF and nominate TIFF-like human fascial fibroblasts as candidate drivers of disease pathology.

Discussion

We have found that early life inflammation can cause Th2 cell accumulation in a unique niche of the skin subcutis that is underpinned by a stromal cell type that we refer to as Th2-interacting fascial fibroblasts (TIFFs). Th2 cytokine exposure drives TIFF expansion to form fibrous bands, while priming of the Th2-TIFF niche enhances tissue repair during adulthood. Thus, early life inflammation durably alters the immunologic tone of skin by populating a latent tissue niche with adaptive immune cells absent in naïve tissue.

Single-cell RNA sequencing of various murine organs has uncovered fibroblast subsets that share notable transcriptional similarities with TIFFs and express varying combinations of markers such as *Dpp4*, *Wnt2*, *Pi16*, *Anxa3*, and *Ill3ral*²⁶⁻³⁰. These stromal cells are found in the adventitia surrounding large neurovascular structures, organ capsules, and body cavity linings^{9,26-28} and appear primed to support type 2 immunity in certain tissues.³¹ Although a

variety of nomenclature has been used in different organs (adventitial cells, mesenchymal stromal cells, adipose stem/progenitor cells, etc.), “boundary fibroblast” may be a broadly applicable term for these cells in that they are located at internal borders which maintain proper compartmentalization of internal organs and vasculature. These boundaries are disrupted by penetrating injuries and/or helminth infections; teleologically, boundary fibroblasts would thus be logical sentinels of interorgan damage that could trigger type 2 immune responses directed at stromal defense and repair. Our discovery of TIFFF-like fascial fibroblasts (fFB) clusters in human skin suggests that the core biology of these cells is conserved. Further exploration of this unique immune-stromal compartment may therefore yield disease-relevant therapeutic strategies and biological insights into the immunology of connective tissues throughout the body.

Methods

Animals

All animals were bred and maintained in a specific pathogen free mouse facility in accordance with the Laboratory Animal Resource Center and Institutional Animal Care and Use Committee of the University of California San Francisco (UCSF). Mice were socially housed under a 12 hour day/night cycle at 25°C and ambient humidity. Littermate controls were used for all experiments, and animals of both sexes were included. Sex, parental cage, and weaning cage were randomized among experimental groups. Strains used in this study include *FoxP3^{DTR}* (*Foxp3^{tm3(DTR-GFP)Ayr}*); *Il5^{Red5}* (*Il5^{tm1.1(icre)Lky}*); *Il4/13^{-/-}* (*Il4/Il13^{tm3Anjm}*); *Il33^{H2B-mCherry 32}*; *Tg(Pdgfra-cre)^{IClc}*; *Il4ra^{tm2Fbb}*; *Fgf18^{CreERT2 33}*; *Rosa26^{DTA}* (*Gt(ROSA)26Sor^{tm1(DTA)Lky}*). All mice were backcrossed onto the C57BL/6J background for at least ten generations.

Human studies

Healthy human samples were collected from normal marginal skin discarded during Mohs Surgery. These de-identified surgical discards were classified as Not Human Subjects Research. Two 6mm full-thickness biopsies of lesional skin (containing subcutaneous fat) were obtained from an eosinophilic fasciitis patient in accordance with a UCSF IRB-approved protocol (17-21582) with informed consent to use the samples for research and to publish de-identified sequencing data. For human histopathologic data, archived, anonymized, paraffin-embedded blocks of healthy eosinophilic fasciitis skin were reviewed by a board-certified dermatopathologist (T.H.M). Healthy control specimens containing at least 30% subcutis by area were selected to match age, sex, and body site of EF cases.

Injection of cytokines and pharmacologic agents

Neonatal Treg depletion: *FoxP3^{DTR}* mice were injected intraperitoneally with two doses of 25 ng/g body weight diphtheria toxin (DT, Sigma D0564) dissolved in PBS at 2.5ng/ μ L concentration (or PBS alone in controls). Injections were spaced one week apart, with the first injection between postnatal days 8-10 (P8-10). Adult Treg depletion followed the same dosing and time course of DT administration, starting during second telogen (7-8 weeks of age).

Cytokine injection: Mice were injected subcutaneously each day with the following cytokines dissolved in 100 μ L PBS: 500ng rmIL-33 (Biolegend 580506) or 500ng rmIL-13 (Biolegend 575906) and 500ng rmIL-4 (Biolegend 715004) complexed with 2.5 μ g anti-mIL-4 (Bio X-Cell 11B11). Whole back skin was harvested for all cytokine injections.

FTY720: FTY720 (Selleck S5002) was diluted in saline and injected intraperitoneally at a dose of 1 μ g/g body weight for the duration of the experiment. 2.5% DMSO was used for control injections.

Additional Models of Th2 Inflammation

For ovalbumin/papain immunization, mice were injected subcutaneously with 100 μ g ovalbumin (Sigma A5503) and 50 μ g papain (Millipore 5125) dissolved in 50 μ L PBS. Two subcutaneous 25 μ L injections were made subcutaneously on the right flank into suprascapular and suprapelvic skin at P8 and P15. Only skin from the injected flank was dissected for analysis. For helminth infection, 100 third-stage *Nippostrongylus brasiliensis* larvae were suspended in 50 μ L PBs and injected at P8. Two subcutaneous 25 μ L injections were into interscapular and suprapelvic back skin along the midline. Th2 responses were boosted at P15 with injection of *Nippo* allergen (200 larvae, freeze-thawed three times³⁴). A ~1cm wide strip of midline back skin was dissected for analysis.

Full-thickness Wounding

All wounding experiments were conducted during second telogen (7-10 weeks old). Prior to wounding, back skin was shaved with clippers. On the day of wounding, mice were anesthetized with 2.5% isoflurane and injected subcutaneously with 50 μ L of 0.25% bupivacaine and 50 μ L of 50 μ g/mL buprenorphine for analgesia. Shaved back skin was then sterilized with a betadine swab and six full-thickness excisional wounds were generated with a 4mm biopsy punch. In some experiments, biopsy tissue was processed for flow cytometry to enable paired pre- and post-wounding analyses. At the time of sacrifice, wounds and adjacent tissue were excised with an 8mm biopsy punch. Wounds were photographed with an in-frame ruler at the indicated timepoints. Wound diameter was quantified with QuPath v0.2.3 image analysis software³⁵, and wound data was fitted to a one-phase exponential decay model in Prism 8 for comparison of the rate constant k between groups (GraphPad).

Tissue Processing

Mouse tissue: After euthanasia, back skin was shaved and dissected. Any remaining scapular or inguinal fat was removed, and the remaining tissue was weighed, finely minced with scissors, placed in a 50mL conical containing 3mL of digestion media (2mg/mL collagenase XI, 0.5mg/mL hyaluronidase, 0.1mg/mL DNase in RPMI with 10% calf serum, 1% HEPES, 1% non-essential amino acids, 1% GlutaMAX, and 1% penicillin-streptomycin), and digested in a bacterial shaker for 45 minutes at 37°C and 225rpm. Digestion was then quenched with 10mL of cold RPMI and samples were vortexed for 10 seconds and strained successively through 100 μ m and 40 μ m strainers. The resulting single cell suspension was then plated in 96-well plates for staining. In indicated experiments, skin was dissected into an epidermal/dermal fraction and a subdermal fraction by pinning the skin tautly and roughly scraping off the subcutis with forceps

until no dermal adipose tissue remained. For lymph node samples, axillary, brachial, and inguinal lymph nodes (“sdLN”, collectively) were dissected and mashed through a 100µm filter with a 5mL syringe plunger into cold media.

Human tissue: Punch biopsies and surgical excisions were finely minced with scissors and incubated in a digestion cocktail containing collagenase IV (0.8 mg/mL, Worthington, LS004186) and DNase (20 µg/mL, MilliporeSigma, DN251G) diluted in RPMI with 10% fetal bovine serum, 1% HEPES, 1% non-essential amino acids, 1% Glutamax, and 1% penicillin-streptomycin. The next morning, digests were briefly shaken and passed through a 100µm strainer to yield a single-cell suspension. Red blood cells were lysed with a 5 minute room-temperature incubation in BD PharmLyse (BD 555859) following manufacturer instructions before proceeding to antibody staining for FACS sorting.

Flow cytometry

Single-cell suspensions were pelleted and resuspended in PBS with 2% FBS containing fluorophore-conjugated antibodies. Cells were initially stained with antibodies targeting cell surface proteins and Ghost 510 viability dye (Tonbo Biosciences 13-0870) for 30min on ice and washed with PBS containing 2% FBS. For biotinylated antibodies, a subsequent 15min incubation with fluorophore-conjugated streptavidin was used. For intracellular target staining, cells were then fixed and permeabilized using the Cytofix/Cytoperm kit (BD Biosciences 554714). For experiments involving intracellular cytokine staining (ICS), single cell suspensions were plated at 4×10^6 cells/well in a 96-well round bottom plate, resuspended in 1X cell stimulation cocktail (Tonbo Biosciences TNB-4975), and incubated at 37°C for 4 hours before antibody staining. Samples were run for analysis on a BD Fortessa or sorted on a BD FACS Aria2.

The following antibodies were used for mouse flow cytometry: CD16/32, a.k.a. Fc Block (Bio X Cell BE0307, clone 2.4G2, 1:100), CD26-PerCP-Cy5.5 (eBioscience 45-0261-82, clone H194-112, 1:100); CD9-FITC (eBioscience 11-0091-82, clone KMC8, 1:100); CD9-Alexa 647 (Biolegend 124809, clone MZ3, 1:100); PDPN-PE-Cy7 (eBioscience 25-5381-82, clone 8.1.1, 1:200); EpCAM-APC-eFluor780 (eBioscience 47579182, clone G8.8, 1:200); CD45-Alexa 700 (eBioscience 56045182, clone 30-F11, 1:200); CD34-Alexa 647 (BD 560230, clone RAM34, 1:100); CD140a-BV650 (BD 740531, clone APA5, 1:100); Sca-1-BV605 (Biolegend 108133, clone D7, 1:100); CD31-BV421 (BD 563356, clone 390, 1:400); IL4RA-biotin (BD 552508, 1:100); CD90.2-PerCP-Cy5.5 (Biolegend 140322, clone 30-H12, 1:500); CD49d-PE-Cy7 (Biolegend 103618, clone R1-2, 1:200); CD3e-APC-eFluor780 (eBioscience 47003182, clone 145-2C11, 1:100); CD3e-BV711 (BD 563123, clone 145-2C11, 1:100); IL-18R1-APC (eBioscience 17-5183-82, clone P3TUNYA, 1:200); CD8a-BV785 (Biolegend 10050, clone 53-6.7, 1:200); CD4-BV650 (BD 563747, clone RM4-5, 1:200); CD69-BV605 (Biolegend 104530, clone H1.2F3, 1:100); Ghost Fixable Vital Dye 510- (Tonbo 130870); ST2-biotin (MD Bioscience 101001B, clone DJ8); Streptavidin-eFluor 450 (eBioscience 48431782); Streptavidin-PE (BD 554061); TCRgd-PerCP-Cy5.5 (Biolegend 118118, clone GL3, 1:200); Ly6G-PE-Cy7 (Biolegend 127618, clone 1A8, 1:200); Siglec F-PE (BD552126, clone E50-2440, 1:200); CD11b-APC-eFluor780 (eBioscience 47011282, clone M1/70, 1:200); CD64-BV785 (BD 741024, clone X54-5/7.1, 1:100); CD11c-BV650 (Biolegend 117339, clone N418, 1:100); Ly6C-BV605 (BD 563011, clone HK1.4, 1:100); MHC-II-eFluor 450 (eBioscience 48532182, clone M5/114.15.2, 1:400); Arg1-APC (eBioscience A1exF5, 17-3697-82, 1:100); CD103-PE-CF594 (BD 565849, clone M290, 1:200); TCRb-PerCP-Cy5.5 (Tonbo 655961-U100, clone H57-597, 1:200); IL-17A-PE-Cy7 (eBioscience 506922, clone eBio17B7, 1:100); IL-13-PE

(eBioscience 12-7133-82, clone eBio13A, 1:100); IL-5-APC (Biolegend 504306, clone TRFK5, 1:100); IFN γ -BV650 (Biolegend 505831, clone XMG1.2, 1:100); FoxP3-eFluor 450 (eBioscience 48577382, clone FJK-16s, 1:100); Ki67-AF488 (Invitrogen 14-5698-82, clone SolA15, 1:100). For flow cytometry of human samples, the following antibodies were used: CD324-PerCP-Cy5.5 (BD 563573, clone 67A4, 1:100); CD31-APC-eFluor 780 (eBioscience 47-0319-42, clone WM59, 1:100); CD45-BV650 (Biolegend 304044, clone HI30, 1:100); CD235a-Pacific Blue (Biolegend 349108, clone HI264, 1:100); Ghost Fixable Vital Dye 510- (Tonbo 130870); CD90-PE (BD 555596, clone 5E10, 1:500).

For all cell types, initial forward scatter vs. side-scatter gates were carefully adjusted by backgating on live CD45⁺ and/or live PDPN⁺ populations to include all cells and exclude debris. Strict dead cell and doublet exclusion was performed prior to gating for immune cells (CD45⁺) and/or stromal cells (CD45⁻ CD31⁻ Ter119⁻ EpCAM⁻, collectively “Lin⁻”). T cells were gated as CD45⁺ CD3^{mid} (excluding CD3^{hi} dendritic epidermal T cells) and subsetted into CD4 T effs (CD4⁺ FoxP3⁻), Tregs (CD4⁺ FoxP3⁺), CD8 T cells (CD8⁺), and dermal $\gamma\delta$ T cells (CD4⁻ CD8⁻ TCR $\gamma\delta$ ⁺). The GFP-DTR fusion protein in *FoxP3-DTR* mice was used to report FoxP3 expression. In mice bearing the *Il5^{Red5}* allele, Th2 cells were identified as CD4⁺ FoxP3⁻ tdTomato⁺, and CD4⁺ FoxP3⁻ tdTomato⁻ cells are referred to as bulk T effectors. ILC2s were gated in these mice as CD45⁺ CD3⁻ CD4⁻ CD8⁻ Thy1⁺ tdTomato⁺, as described ⁵. Eosinophils were identified as CD45⁺ Ly6G⁻ CD11b⁺ Siglec F⁺ and neutrophils were identified as CD45⁺ Ly6G⁺ MHCII⁻. Macrophages (CD64⁺ CD11b⁺ CD11c⁻), monocytes (Ly6C⁺ within the macrophage gate), alternatively activated macrophages (Arg-1⁺ within the macrophage gate), and dendritic cells (CD64⁻ MHCII⁺ CD11c⁺) were gated after excluding T cells, B cells, eosinophils, and neutrophils. Within the Lin⁻ stromal gate, CD34⁺ Sca1⁺ cells are denoted “bulk fibroblasts”

as they are ~80% PDPN⁺ and PDGFR α ⁺ in P21 mouse skin, in contrast to CD34⁻ Sca1⁻ “non-FB stroma.” Within the bulk FB gate, TIFFs were gated as CD26⁺ CD9^{lo-mid}. Cell numbers were calculated either using CountBright counting beads (ThermoFisher C36950) or by quantifying cell numbers on a NucleoCounter (ChemoMetec) prior to staining. All flow cytometry analysis was performed using FlowJo v10.7 or FlowJo v9.9.6 (BD).

Thin-section Immunofluorescence Microscopy

Shaved back skin was placed fat side-down on a paper towel, cut into 3mm-width sagittal strips, and fixed in 4% paraformaldehyde on a rocker for either 1 hour at room temperature or 4°C overnight. After three washes in PBS, skin strips were rolled into a spiral with forceps, embedded in optical cutting temperature compound (OCT), and flash-frozen in absolute ethanol cooled with dry ice. 12 μ m sections were cut on a cryostat (ThermoFisher Cryostar NX50) on SuperFrost Plus slides and stored at -20°C until staining. For antibody staining, frozen sections were air-dried for one hour, washed in PBS, blocked for 30 minutes in PBS with 10% FBS, 5% donkey serum, and 0.3% Triton X-100, then stained with the following antibodies diluted in blocking buffer overnight at 4°C: dsRed (Takara rabbit polyclonal 632496, 1:200); perilipin-1 (Cell Signaling 349108, rabbit clone D1D8, 1:500); CD3e (Biolegend 100202, rat clone 17A2, 1:100); CD26 (R&D goat polyclonal AF954, 1:100); Myosin IV-AF488 (Invitrogen 53650382, mouse clone MF20, 1:100); ER-TR7-AF647 (Santa Cruz 73355-AF647, 1:200); and keratin-14 (Biolegend 906001, chicken polyclonal, 1:400); GATA3 (Cell Marque 390M-17, mouse clone L50-823, predilute); CD4 (Dako 104R-17, rabbit clone SP35, predilute).

After washing in PBS, sections were stained for 2h at room temperature in the following secondary antibodies diluted 1:500 in blocking buffer: donkey anti-rabbit Alexa 555 (Invitrogen A31572), donkey anti-goat Alexa 647 (Invitrogen A21447), donkey anti-rat Alexa 647 (Jackson

ImmunoResearch 712605153), donkey anti-rabbit Alexa 488 (Invitrogen A21206), and/or donkey anti-rat Alexa 488 (Invitrogen A21208). Sections were washed three more times in PBS and mounted in ProLong Gold antifade reagent (ThermoFisher P10144) and imaged on a Zeiss M2 Imager with an Apotome attachment.

Thick-section Confocal Microscopy

Back skin was dissected and frozen as above and 100-200 μ m sections were cut on a cryostat and transferred into PBS with forceps. Sections were then stained in a 48-well plate using the antibodies above with double the incubation and wash times and transferred between wells with forceps, taking care not to disrupt the fascia. Sections were mounted on slides in refractive index matching solution (RIMS, see Yang et al., 2014), using a dissection microscope to preserve orientation. Imaging was conducted on either a Leica SP8 scanning confocal microscope with a white light laser and 20x/0.8NA multi-immersion objective; a Zeiss M2 imager with Apotome attachment and 20X/0.8NA air objective; or a Nikon A1r scanning confocal microscope with 405nm, 488nm, 561nm, and 633nm lines and a 20x/1.0NA water objective at approximately 0.4 x 0.4 x 0.8 μ m resolution.

Image Analysis

For quantification of Th2 and ILC2 localization in skin, Imaris 9.3 (BitPlane) was used to analyze confocal imaging data from *Il5^{Red-5/+}*; *Rosa26^{tdTomato}*; *FoxP3-DTR* mice, in which IL-5 reporter signal is boosted by additional Cre-mediated recombination and tdTomato expression from the Rosa26 locus. Th2 and ILC2 cells were identified using Imaris's Surface tool to segment tdTomato+ cells, and then these two cell types were distinguished by thresholding on CD3 intensity within each cell object. The skin epidermis, dermis, dermal adipose tissue,

panniculus carnosus, and fascia were then segmented by manually drawing surface contours on each z-plane, and cell localization was determined by creating a distance mask to each layer.

Quantification of GATA3⁺ CD4⁺ T cells in human IHC sections was performed using Qupath v0.2.3.³⁵ Small representative ROIs of hematoxylin, DAB (GATA3), alkaline phosphatase (CD4), and background were used to set stain vectors. Cells were detected with the watershed algorithm-based “Detect Cells” tool, using the optical density sum to segment nuclei with a cytoplasmic expansion of 1.5 μ m. Cells were then classified with the “Train Object Classifier Tool,” using a neural network trained on 15-30 annotations of each cell class (GATA3⁺ CD4⁺, GATA3⁺ CD4⁻, and CD4⁻) with the following features as input: nuclear GATA3 mean/std dev, nuclear hematoxylin mean/std dev, nuclear CD4 mean/std dev, cytoplasmic GATA3 mean/std dev, and cytoplasmic CD4 maximum. Dermis and subcutis were manually annotated for cell localization, and tissue area was detected with a simple threshold.

RNA Preparation and qPCR

Sorted, pelleted fibroblast populations ($10^4 - 10^5$ cells) were snap frozen, and RNA extraction was conducted with the PureLink RNA Mini kit (ThermoFisher 12183020). cDNA synthesis was performed with the iScript Advanced cDNA kit (Bio-Rad 1725038), pre-amplification with the SsoAdvanced Preamp kit (Bio-Rad 1725160). qPCR was carried out with the PrimeTime Gene Expression master mix (IDT 1055772) on a StepOnePlus real-time PCR system (Applied Biosystems) under fast cycling conditions using the following Taqman primers: Anxa3-FAM (Mm00442685), Il13ra1-FAM (Mm01302068), Wnt2-FAM (Mm00470018), and Gapdh-VIC (Mm03302249).

Fibroblast-Th2 Co-cultures

For fibroblast isolation, back skin was dissected from mice in first telogen (P19 – P25) and separated into dermal and subdermal fractions as above. Each fraction was sorted separately on a BD FACS Aria 2, with dermal FBs sorted from the dermal fraction ($\text{Lin}^- \text{CD34}^+ \text{Sca1}^+ \text{CD26}^{+/-} \text{CD9}^+$) and TIFFs sorted from the subdermal fraction ($\text{Lin}^- \text{CD34}^+ \text{Sca1}^+ \text{CD26}^+ \text{CD9}^-$). Fibroblasts were plated separately in a 96-well flat-bottom plate (10,000 per well) in DMEM with 10% fetal bovine serum, 1% GlutaMAX, and 1% penicillin/streptomycin and grown to confluence over 6 days. For Th2 cell purification, neonatal *Il5^{Red5/+}; FoxP3^{DTR}* mice were Treg depleted as above and treated with three subcutaneous injections of 500ng IL-33 at approximately P21 – 25 to boost Th2 numbers. Whole skin was dissected at P27-28 and $\text{CD3}^+ \text{CD4}^+ \text{FoxP3}^- \text{IL5}^{\text{tdTomato}^+}$ skin Th2 cells were FACS-purified. Sorted Th2 cells were labeled with 2.5 μM CellTrace Violet (ThermoFisher C34557) following manufacturer instructions and then cultured with confluent fibroblasts for four days before harvest. In some conditions, Th2 cells were cultured in media alone or media supplemented with IL-2 (Biolegend 589104, 200U/mL), IL-7 (20ng/mL, 577802), and IL-33 (20ng/mL, 580502).

Mouse Single-Cell RNA Sequencing

Stromal cells ($\text{CD45}^- \text{CD31}^- \text{Ter119}^- \text{EpCAM}^-$) from back skin digest of control or $\Delta\text{neoTreg}$ mice at P22 were run on a BD FACSAriaII using a 100 μm nozzle and sorted into RPMI + 10% FBS. Two male mice were pooled per group, and samples were run on separate lanes of a 10X Chromium chip with 3' v2 chemistry (10X Genomics) following manufacturer instructions by the UCSF Institute for Human Genetics Sequencing Core. Libraries were sequenced on an Illumina Novaseq 6000. Fastq files were aligned to the mm10 reference genome and barcode matrices were generated using Cellranger 2.1.

Downstream data analysis, including clustering, visualizations, and exploratory analyses, were performed using Seurat 3.2.0. Cells with <200 features, >25,000 reads, or >6% mitochondrial genes were filtered out during preprocessing. The Seurat `SCTransform` function was applied to each dataset, and the data were integrated using the canonical correlate analysis based `IntegrateData` function with the top 3000 most variable features selected as SCT integration anchors. PCA and UMAP were run on the integrated object, and an initial low-resolution clustering was generated using the first 20 principal components. Based on this preliminary clustering, the following populations of contaminating cell types were removed based on the expression of the indicated markers: keratinocytes (*Krt5*, *Krt14*, *Cdh1*), immune cells (*Ptprc*), endothelial cells (*Pecam1*, *Cdh5*), melanocytes (*Mlana*, *Tyr*), skeletal muscle cells (*Acta1*, *Des*), and red blood cells (*Alas2*). The subsequent filtered dataset containing fibroblast and mural cell types was split and the `SCTransform`-based integration pipeline was re-run with new variable features selected as anchors. The final integrated object was clustered using the first 20 principal components and a resolution of 0.4. Markers for each cluster were identified with the Seurat `FindAllMarkers` functions using a Wilcoxon rank sum test and corrected for multiple testing with the Bonferroni method. Markers of TIFFs with an average \log_2 fold change > 0.25 were used to construct the TIFF signature used in cross-tissue met-analysis, described below (n = 313).

For comparison of TIFFs to stromal cells types in other tissues, cross-tissue steady-state mouse fibroblast atlas data analyzed in Buechler et al⁹ was downloaded from fibroXplorer.com as a Seurat object in RDS format (v0.3.0). The TIFF module score of each cross-tissue fibroblast cluster was calculated with the Seurat `AddModuleScore` function. Gene set enrichment of the TIFF signature within each fibroblast cluster from Buechler et al was calculated using the

geneset enrichment analysis (GSEA) algorithm implemented in the fgsea R package with parameters `scoreType = "pos"`, `eps=1e-100`, and `nproc=1`.

Human Single-Cell RNA Sequencing

Single-cell suspensions obtained from digest of full-thickness human skin biopsies were run on a BD FACSAriaII using a 100µm nozzle. Stromal cells (CD45⁻ CD31⁻ E-cadherin⁻ CD235a⁻) were sorted from into RPMI + 10% FBS, using Thy-1 as a “positive control” gate to fine-tune the separation of Lin⁻ cells from debris via backgating. Samples were submitted to the UCSF Institute for Human Genetics Sequencing Core, where they were loaded onto a 10X Chromium chip with 3’v3 chemistry (10X Genomics) following manufacturer instructions and sequenced on an Illumina HiSeq 4000. Fastq files were aligned to GRCh38 with Cell Ranger version 3.0.2.

Downstream data analysis, including clustering, visualizations, and exploratory analyses, were performed using Seurat 3.1.2. Cells with <200 features, >30,000 reads, or >6% mitochondrial genes were filtered out during preprocessing. The Seurat `SCTransform` function was applied to each dataset, and the data were integrated using the canonical correlate analysis based `IntegrateData` function with the top 3000 most variable features selected as SCT integration anchors. PCA and UMAP were run on the integrated object, and an initial low-resolution clustering was generated using the first 50 principal components. Based on this preliminary clustering, the following populations of contaminating cell types were removed based on the expression of the indicated markers: keratinocytes (*KRT5*, *KRT14*, *DSG1*, *DSG3*), immune cells (*PTPRC*), and endothelial cells (*PECAMI*, *CDH5*). One cluster of cells of uncertain identity expressing very low levels of *PECAMI* and *CDH5* was left in the final analysis shown in Figure 5 and labeled “endothelial.” The subsequent filtered dataset containing

fibroblast and mural cell types was split and the SCTransform-based integration pipeline was re-run with new variable features selected as anchors. The final integrated object was clustered with SNN-based using the first 50 principal components and a resolution of 0.5. Markers for each cluster were identified with the Seurat `FindAllMarkers` function using a Wilcoxon rank sum test and corrected for multiple testing with the Bonferroni method. Data from the eosinophilic fasciitis patient was analyzed in a similar fashion through SCTransform-based integration with healthy samples and SNN-based clustering with 15 PCs and resolution 0.35. Original cell type annotations from the healthy-only analysis were retained in metadata and projected onto the UMAP plot of EF-integrated data to ensure that clusters were being annotated in a similar fashion to the healthy-only analysis (similar to cross-species transcriptomic analysis, see Fig. 5E and methods section below).

Cross-Species Transcriptomic Analysis

In order to directly compare mouse and human scRNAseq data, the control mouse skin samples was re-clustered and analyzed from its counts matrix as described above, and genes within the resulting Seurat object were renamed with their most likely human orthologs. Possible human orthologs for murine genes were retrieved from the Ensembl GRCh38 assembly using the BiomaRt package's `getLDS` function (v2.46). Additional parameters retrieved for each possible ortholog included the orthology confidence score, whole genome alignment score, GOC score, and percentage identity. Orthologs lacking an HGNC symbol were removed from the humanized gene list. For mouse genes with multiple human orthologs, a single ortholog was assigned using the following tiebreaking procedure: confidence=1, highest whole genome alignment score, highest GOC score, percentage base pair identity. A final list of one-to-one mouse-to-human ortholog pairings was used to rename genes within the mouse Seurat object counts matrix.

An initial list of 313 mouse T1FF signature genes was generated from the output of the Seurat `FindAllMarkers` function listed above, thresholded by `avg_logFC > 0.25`, and converted human orthologs as above. This T1FF signature was then filtered to remove genes that were not variably expressed in human data, resulting in a final set of 144 genes. Fisher's Exact Test was run on each human stromal cluster using the base R function `fisher.test`, and p-values were adjusted for multiple comparisons by using the base R function `p.adjust` to apply the Benjamini-Hochberg procedure. The mT1FF module score was calculated by running the Seurat `AddModuleScore` function on the 144-gene mT1FF signature. For generation of the cross-species stromal atlas, original cluster identities of mouse and human cells were stored in the metadata of each Seurat object separately. Integrated human data was then split by sample. SC-transformed mouse and human data were integrated with a newly calculated variable features space. Clustering was performed on the first 50 principal components with resolution 0.4. Visualization of the original mouse and human cluster identities projected onto the cross-species UMAP was performed using the Seurat `DimPlot` function with the cells in each single-species cluster designated in the `cells.highlight` parameter.

Quantification and Statistical Analysis

Statistical analyses were performed using Prism 8 (GraphPad) unless otherwise specified. Detailed testing methods are included in figure legends. All statistical hypothesis testing was performed with two-tailed tests, and significance is displayed across figures using the following legend: * $p < 0.05$, ** $p < 0.005$, *** $p < 0.0005$. With the exception of scRNAseq, all experiments were repeated 2-3 times, and all data points represent individual biological replicates.

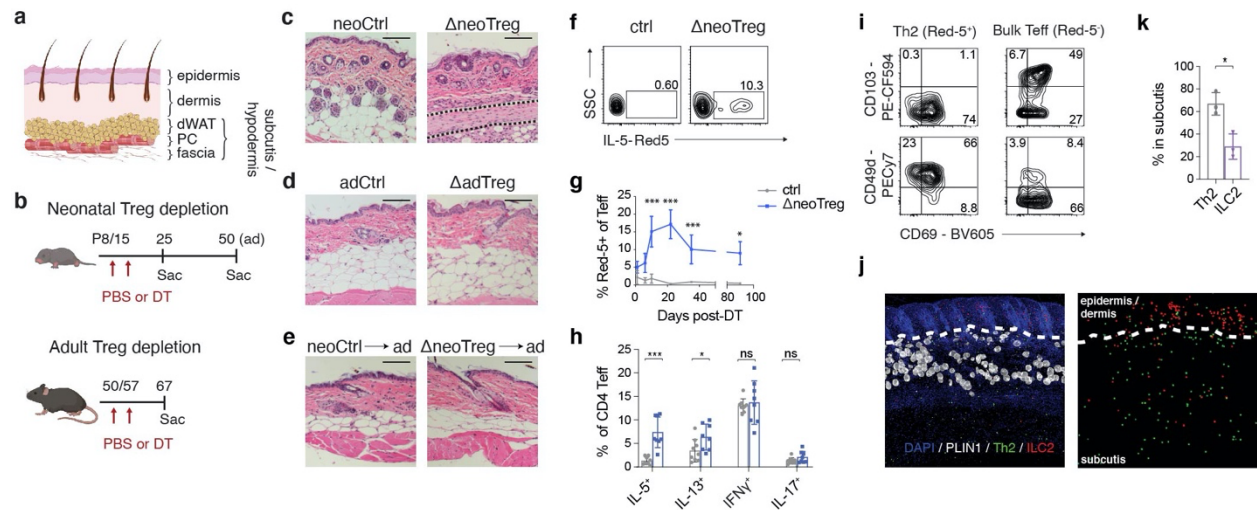


Figure 2.1- Transient neonatal Treg reduction causes temporary derangement of stromal architecture and lasting Th2 accumulation in the skin subcutis.

(a) Anatomic layers of murine skin. dWAT- dermal white adipose tissue; PC- panniculus carnosus. (b-e) *FoxP3^{DTR}* mice were treated with either PBS (Ctrl) or DT at indicated postnatal days and sacrificed at 10 days (c, d) or 35 days (e) post-treatment. Representative skin histology is shown with fibrous bands outlined. Scale bars, 100 μ m. (f-g) Th2 cells in skin from adult (P50) *Il5^{Red5/+}; FoxP3^{DTR}* mice following neoTreg reduction. $n=3-7$ animals per data point (47 total), one experiment per time point. (h) Skin T helper subsets by intracellular cytokine staining at P50. $n=17$ animals. (i) Lymphocyte integrin expression in Δ neoTreg mice at P50. (j-k) Th2 and ILC2 localization in skin of Δ neoTreg *Il5^{Red5/+}; Rosa26^{tdTomato/+}; FoxP3^{DTR}* mice. Cells were segmented by tdTomato and CD3 expression. $n=3$ animals. Data are displayed as mean \pm SD from one independent experiment, representative of 2-3 repeats (b-j). * $p < 0.05$, ** $p < 0.01$, *** $p < 0.001$ (all two-sided); two-way ANOVA with Šídák multiple comparison test (g-h); Student's t-test (k).

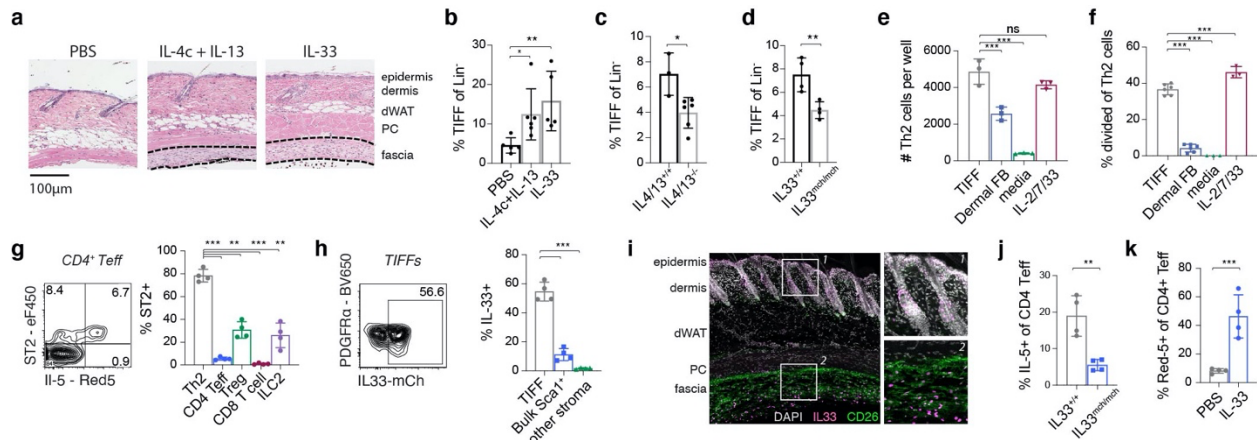


Figure 2.3- Reciprocal interactions between skin Th2 Cells and *Il13ra1*⁺ fibroblasts (TIFFs) drive fascial expansion and Th2 maintenance

(a-b) Control mice were treated with subcutaneous IL-33 or complexed IL-4/ α -IL-4 with IL-13 from P15-P21. Dotted lines denote fascial expansion. $n=16$ animals. (c-d) Flow cytometric TIFF quantification after neoTreg depletion in *Il4/Il13*^{-/-}; *FoxP3*^{DTR} and *Il33*^{-/-}; *FoxP3*^{DTR} mice. $n=9$ animals (c), 8 animals (d). (e-f) TIFFs and dermal fibroblasts were sorted from P21 mouse skin and co-cultured with sorted IL-5^{Red5+} skin Th2 cells from P28 Δ neoTreg mice for four days. $n=12$ samples (e), 18 samples (f). (g-h) Lymphocyte ST2 expression and stromal IL-33 expression in Δ neoTreg mice at P50. $n=4$ animals. (i) Control *Il33*^{mch/+} skin at P50. (j) Skin Th2 frequency in Δ neoTreg mice crossed to the IL-33 deficient *Il33*^{mch/mch} background. $n=8$ animals. (k) Skin Th2 frequency in Δ neoTreg mice that were aged to adulthood and treated with subcutaneous PBS or IL-33. $n=8$ animals. Data are displayed as mean \pm SD from one independent experiment, representative of 2-3 repeats (a-k). * $p < 0.05$, ** $p < 0.01$, *** $p < 0.001$ (all two-sided); Welch ANOVA with Dunnett multiple comparison test (b, e-h); Student's t-test (c-d, j-k).

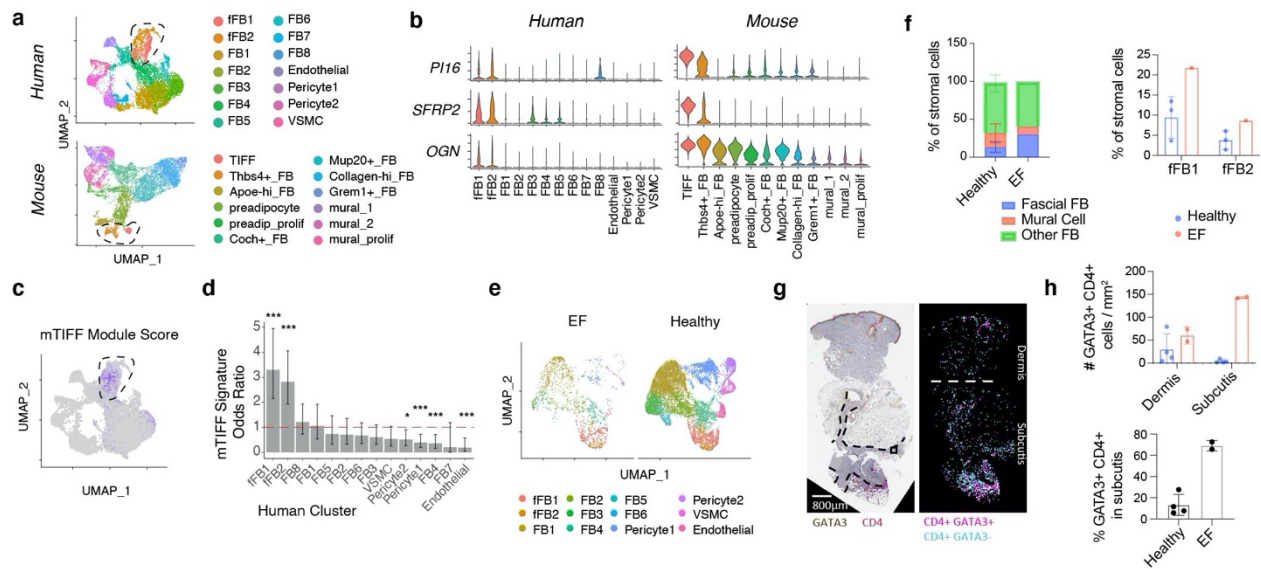


Figure 2.4- T1FF-like cells are present in healthy human skin and in a fibroinflammatory disease of the fascia.

(a) Unsupervised clustering of scRNAseq from FACS-purified stromal cells in healthy human skin ($n = 3$ donors) and control murine back skin (genes converted to human orthologs). **(b)** Expression of murine T1FF (mT1FF) markers in human skin stroma. **(c)** Module score for the mT1FF signature in human stromal cells. **(d)** Enrichment of the mT1FF signature in each human stromal cluster. **(e)** Integration of stromal cells sequenced from eosinophilic fasciitis skin ($n=1$ donor) with healthy controls. **(f)** Frequency of major stromal cell types in healthy and EF skin. $n=4$ donors. **(g-h)** GATA3⁺ CD4⁺ T cell localization in EF skin and controls. Areas of expanded fascia are outlined with dotted lines. $n=6$ samples. Data are displayed as mean +/- SD from one independent experiment (a-h). * $p < 0.05$, ** $p < 0.01$, *** $p < 0.001$ (all two-sided); Fisher's Exact Test with Benjamini-Hochberg correction (d).

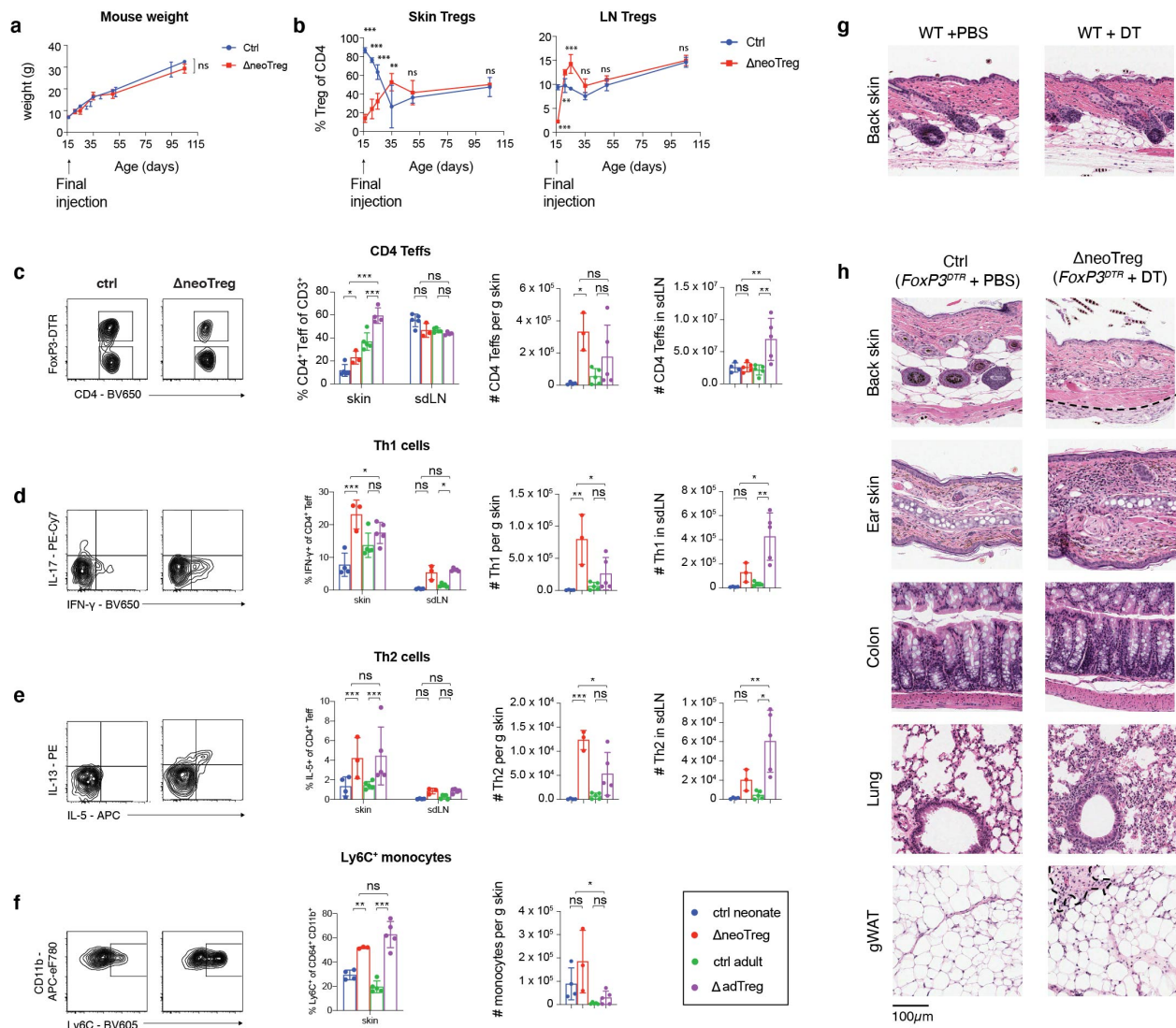


Figure S2.1- Characteristics of cutaneous inflammation induced by neonatal Treg reduction.

(a) Weights of PBS- and DT-treated *FoxP3^{DTR}* mice from the time of treatment to adulthood. $n=3-7$ mice per data point, 51 total. (b) Quantification of Tregs in skin and skin-draining lymph nodes (sdLN) following neoTreg depletion. $n=3-9$ animals per data point (60 total), 1 experiment per time point. (c-f) Representative flow cytometry and quantifications of immune cell populations in skin and skin-draining lymph nodes during the inflammatory phase of neonatal Treg depletion at P25 and adult Treg depletion at P67 (both 10 days after DT). *Gating*: CD8 T cells (CD3⁺ CD8⁺); CD4 Teffs (CD3⁺ CD4⁺ FoxP3⁻); Ly6C monocytes (Ly6C⁺ Siglec F⁻ CD64⁺ CD11c⁻ CD11b⁺ Ly6C⁺). $n=18$ animals. (g) Representative histology of wildtype neonatal mice treated with PBS or DT and sacrificed 10 days post-injection. (h) Histology of selected organs in ΔneoTreg and control mice at P25. gWAT – perigonadal white adipose tissue. Data are displayed

as mean +/- SD from one independent experiment, representative of 2-3 repeats. * $p < 0.05$, ** $p < 0.01$, *** $p < 0.001$ (all two-sided); repeated measures two-way ANOVA (a); two-way ANOVA with Šídák multiple comparison test (b-c); one-way ANOVA with Tukey's multiple comparisons test (c-f).

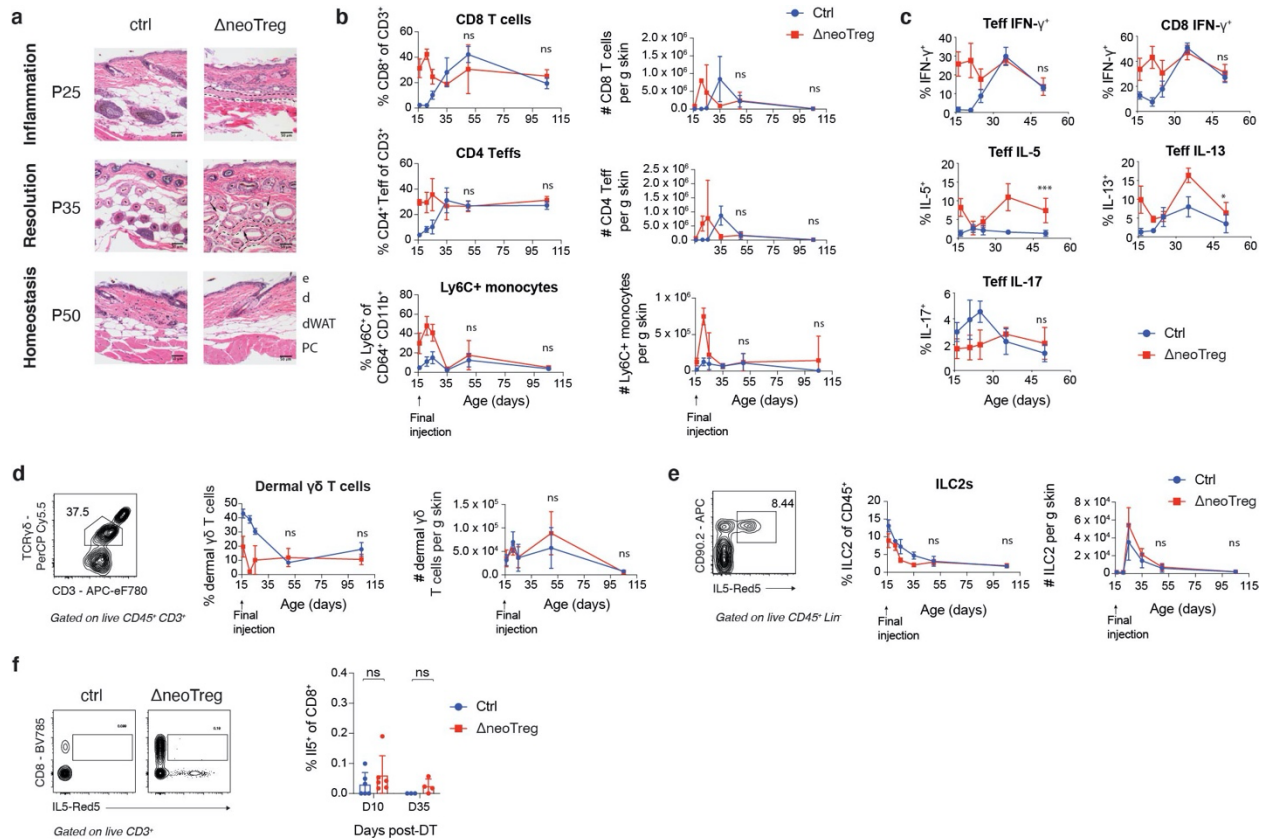


Figure S2.2- Resolution of inflammation and return to homeostasis following neonatal Treg reduction.

(a) Representative skin histology of control and neonatal Treg-depleted *FoxP3^{DTR}* mice at P25, P35, and P50 (10, 20, and 35 days post-DT treatment). Fibrous bands are outlined with dotted lines and regenerating adipocytes are marked by arrows. **(b)** Abundance of selected inflammatory immune cell populations in skin 0-90 days after neoTreg depletion. *n*=3-9 animals per data point (60 total), 1 experiment per time point. **(c)** T helper and CD8⁺ T cell cytokine production 0-35 days after neoTreg depletion, quantified by intracellular cytokine staining. *n*=3-9 animals per data point (51 total), 1 experiment per time point. **(d-f)** Sample gating and quantification of dermal $\gamma\delta$ T cells, ILC2s, and Tc2 cells 0-90 days after neoTreg depletion in *Il5^{Red5/+}; FoxP3^{DTR}* mice. *n*=3-9 animals per data point (51 total, d-e); 3-6 animals per data point, (19 total, f), 1 experiment per time point. Data are displayed as mean \pm SD from one independent experiment, representative of 2-3 repeats. **p* < 0.05, ***p* < 0.01, ****p* < 0.001 (all two-sided); Student's t test at selected time points during adulthood (b-e); two-way ANOVA with Šídák multiple comparison test (f). All results were reproduced over 2-3 independent experiments.

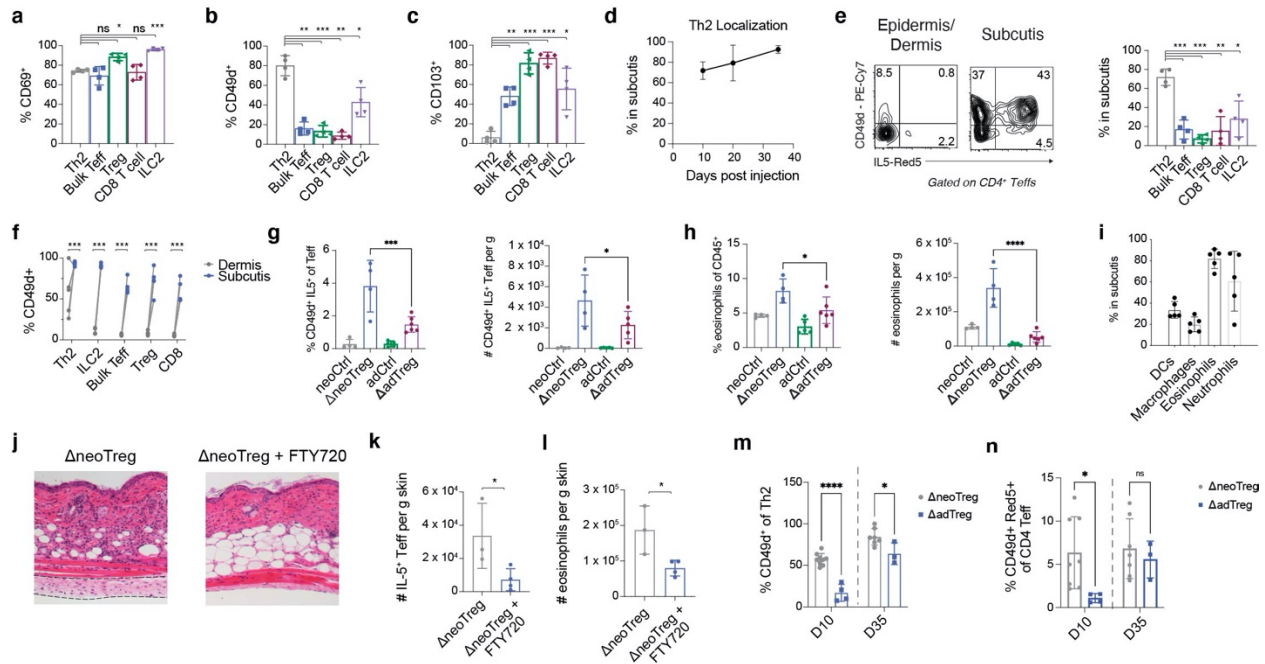


Figure S2.3- CD49d marks subcutis-resident Th2 cells that are associated with subdermal eosinophilia and age-specific fibrous band formation. (a-c) Expression of CD69, CD103 (α_E integrin), and CD49d (α_4 integrin) on skin lymphocytes in Δ neoTreg mice aged to adulthood. Bulk Teff defined as IL5^{Red5-} FoxP3⁻ CD4⁺ T cells. $n=4$ animals. (d-f) Δ neoTreg mice were aged to adulthood, subcutis was separated from the dermis/epidermis, and the two skin fractions were analyzed separately by flow cytometry. Th2 localization over time (d), lymphocyte localization at P50 (e), and CD49d expression in dermal vs. subdermal lymphocytes (f) is shown. $n=4-5$ animals per data point, 14 total (d); 4 animals (e); 5 animals (f). (g-i) Quantification of CD49d⁺ Th2 cells (g) and eosinophils (h) in Δ neoTreg and Δ adTreg mice during the inflammatory phase of Treg reduction at 10 days post-DT. Myeloid cell localization in Δ neoTreg mice (i) was quantified by flow cytometry of dissected skin layers. $n=19$ animals (g-h); 5 animals (i). (j-l) Δ neoTreg mice were treated every other day with FTY720 or vehicle from P8 to P25. Histology (j), Th2 numbers (k), and eosinophil numbers (l) are shown at P25. $n=7$ animals. (m-n) CD49d expression on IL5-Red5⁺ Th2 cells and frequency of CD49d⁺ Th2 cells in Δ neoTreg and Δ adTreg mice during (D10 / P25) and after (D35 / P50) inflammation. $n=23$ animals. Data are displayed as mean \pm SD from one independent experiment, representative of 2-3 repeats. * $p < 0.05$, ** $p < 0.01$, *** $p < 0.001$ (all two-sided); repeated-measures ANOVA with Dunnett's multiple comparison test (a-c, e); 2-way repeated-measures ANOVA with Sidak multiple comparison test (f); Welch's ANOVA with Dunnett's multiple comparison test (g-h); Student's t-test (k-n). All results were reproduced over 2-3 independent experiments.

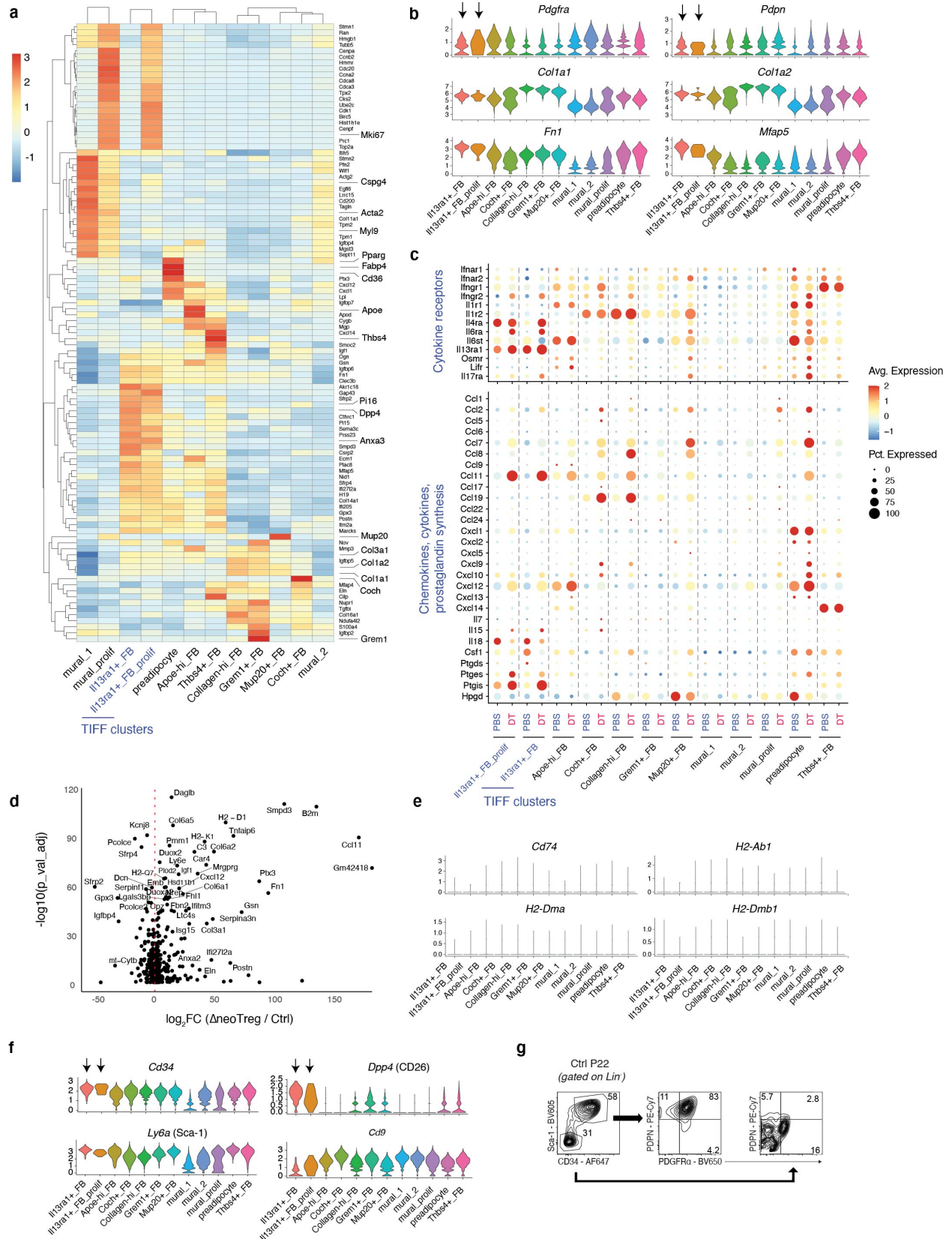


Figure S2.4- Single-cell transcriptomic characterization of skin stroma in control and Δ neoTreg mice.

(a) Expression of marker genes for skin stromal clusters in control mice. **(b)** Expression of fibroblast markers and ECM genes in control mouse skin stroma. **(c)** Expression of immune-related genes in mouse skin stroma, split by control (PBS) and Δ neoTreg (DT) sample. **(d)** Differential gene expression analysis of *Il13ra1*⁺ FBs (TIFFs) in Δ neoTreg vs. control mice. **(e)** Expression of MHC class II-related transcripts in skin stromal clusters (ctrl and Δ neoTreg samples combined). **(f)** Expression of cell surface markers used to design the *Il13ra1*⁺ FB flow cytometry gating strategy in main figure 2d. **(g)** Representative flow cytometry of fibroblast markers PDPN and PDGFR α within subsets of Lin⁻ skin stromal cells from P25 control mice.

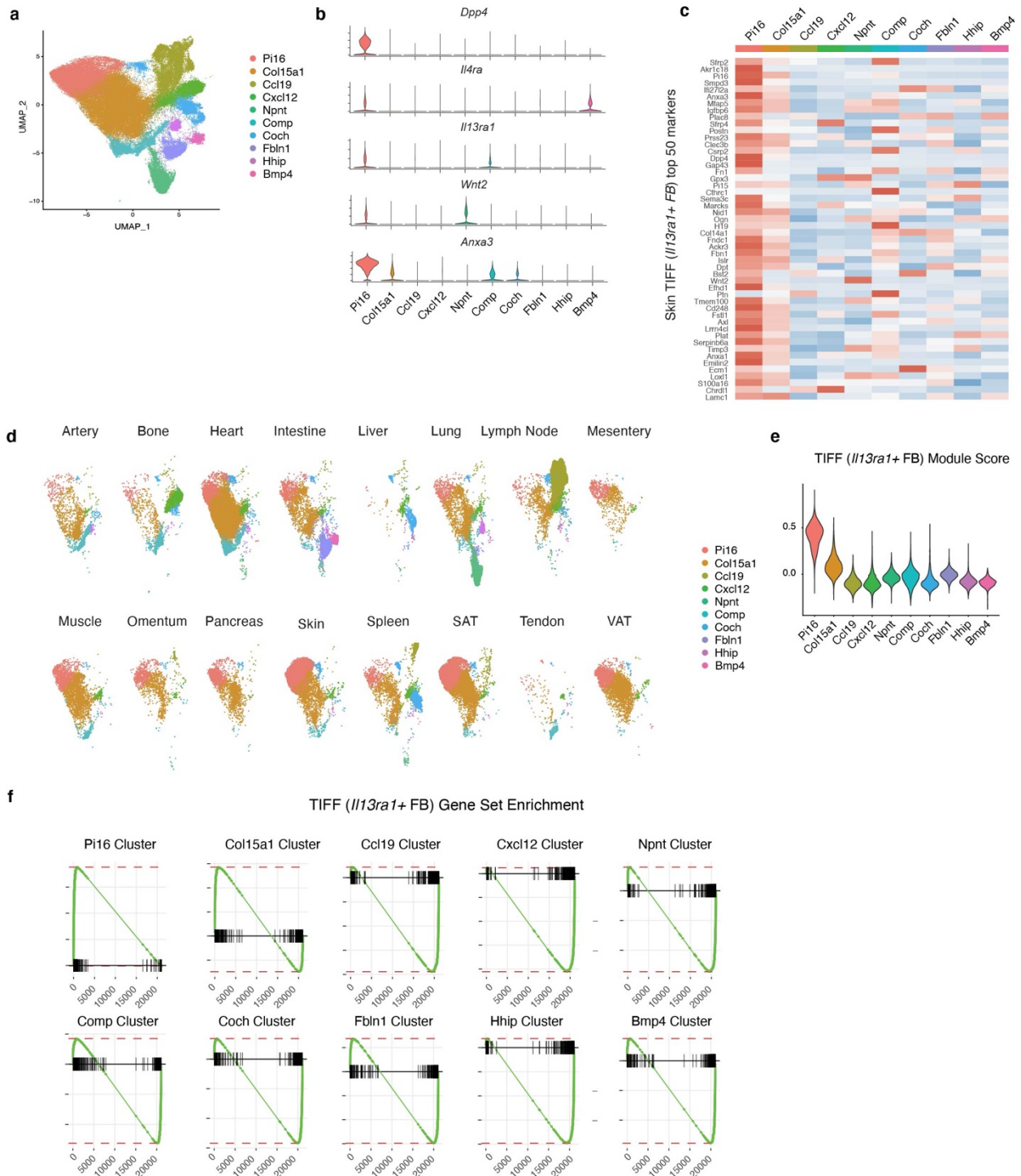


Figure S2.5- *Il13ra1*⁺ FBs / TIFFs are transcriptionally similar to *Pi16*⁺ fibroblasts found across mouse organs.

Published data were downloaded from a mouse cross-tissue fibroblast atlas, containing twenty-eight 10X scRNAseq datasets across 16 murine tissues that were aligned, filtered, and analyzed with a standardized methodology to minimize batch effects.

(a) Steady-state atlas of all 16 tissues was re-plotted, demonstrating similar clustering to

published meta-analysis. **(b)** Expression of TIFF markers from control skin in cross-tissue clusters defined by the atlas. **(c)** Expression of the top 50 TIFF markers (ranked by log-fold change) in cross-tissue atlas clusters. **(d)** Cross-tissue atlas cluster representation in selected tissues. SAT – subcutaneous adipose tissue; VAT – visceral adipose tissue. **(e)** Enrichment of all skin TIFF markers with $\logFC > 0.25$ ($n=313$) among cross-tissue fibroblast atlas clusters, calculated using the Seurat AddModuleScore function. **(f)** Geneset enrichment analysis of the skin TIFF gene set among cross-tissue fibroblast atlas clusters.

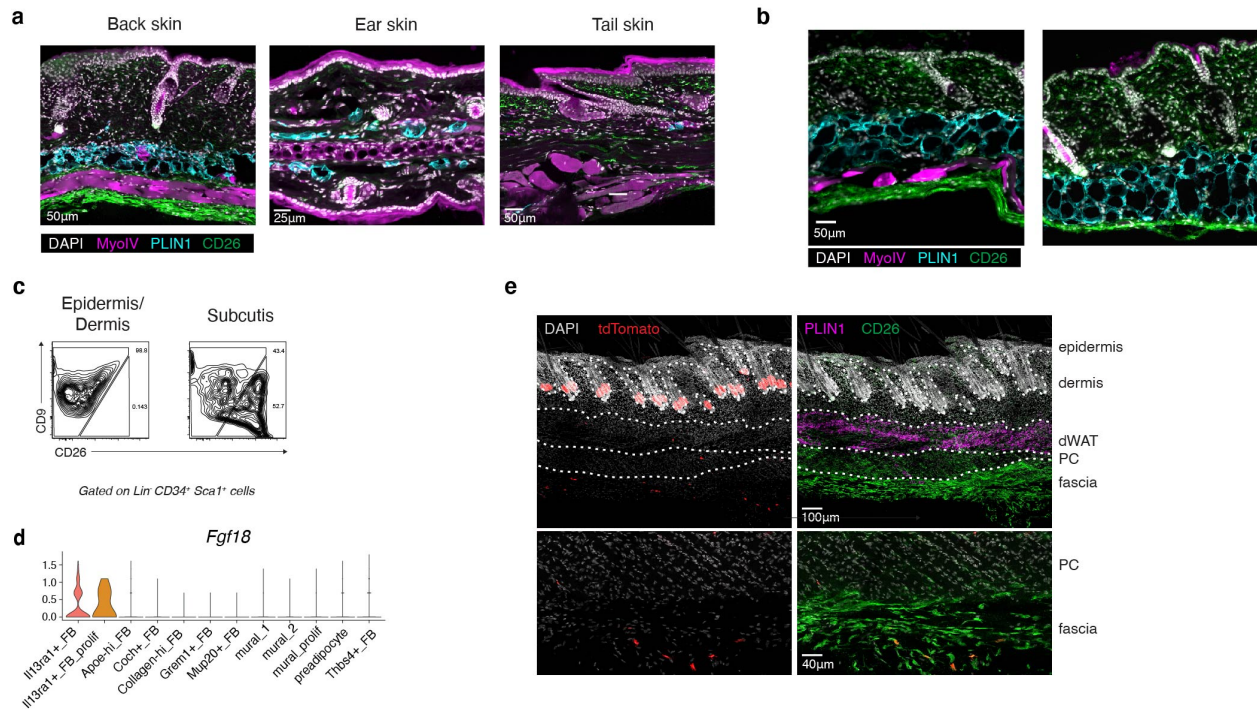


Figure S2.6- Anatomic characterization of *Il13ra1*⁺ fibroblasts (TIFFs)

(a) IF microscopy of mouse back, ear, and tail skin to identify fascia (CD26), adipocytes (PLIN1), and skeletal muscle (MyoIV). **(b)** Variable layering of fascia, adipocytes, and skeletal muscle at two different back skin locations at in P22 control mice. **(c)** Control skin was dissected from P22 mice and the subcutis was manually separated from the dermis and epidermis. *Il13ra1*⁺ FBs (TIFFs) were quantified in each fraction. **(d)** *Fgf18* expression by scRNAseq in control Lin⁻ skin stromal cells. **(e)** Confocal microscopy of adult skin from *Fgf18*^{CreRET2}; *Rosa26*^{tdTomato} mice injected with tamoxifen for five days prior to harvest. *Top row*: Z-projection with tdTomato signal thresholded for visualization. *Bottom row*: inset of fascia with original tdTomato fluorescence. All results were reproduced over 2-3 independent experiments.

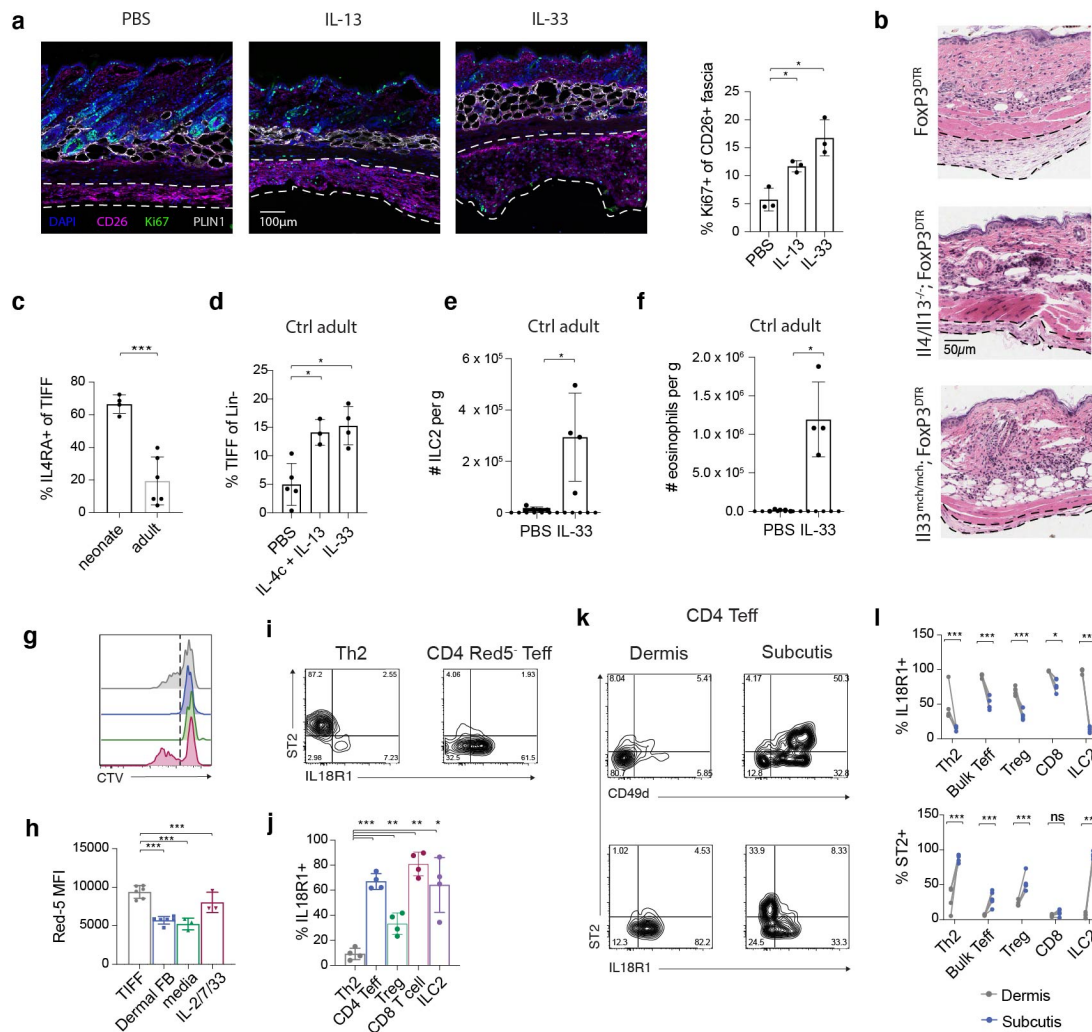


Figure S2.7- Further characterization of Th2-TIFF interactions in the subdermal niche.

(a) IF microscopy of skin from wildtype mice injected for five days with IL-13 or IL-33 starting at P21 with quantification of fascial proliferation by Ki67. $n=9$ animals. (b) Skin histology from Δ neoTreg mice crossed to IL4/13- or IL33-deficient strains at P25 (10 days post-DT). (c) Expression of IL4RA on TIFFs from wildtype neonate (P25) and adult (P50) mice. $n=10$ animals. (d-f) Adult mice were injected for 7 days with type 2 cytokines and the indicated cell populations in skin were quantified by flow cytometry. $n=13$ animals (d); 7 animals (e-f). (g-h) TIFFs and dermal fibroblasts were sorted from P21 mouse skin and co-cultured with sorted IL-5^{Red5+} skin Th2 cells from Δ neoTreg mice for four days. $n=12$ samples (h). (i-j) IL-18R1 and ST2 expression in skin lymphocyte subsets with quantification of IL-18R1 expression (see main fig. 2.3g for ST2). $n=4$ animals. (k-l) Δ neoTreg mice were aged to adulthood, the subcutis was separated from the dermis/epidermis, and expression of alarmin receptors was quantified across lymphocyte subsets. $n=5$ animals. Data are displayed as mean \pm SD from one independent experiment, representative of 2-3 repeats. * $p < 0.05$, ** $p < 0.01$, *** $p < 0.001$ (all two-sided); Welch's ANOVA with Dunnett Multiple Comparisons Test (a, d, h, j); Student's t-test (c, e-f); two-way ANOVA with Šídák multiple comparison test (l).

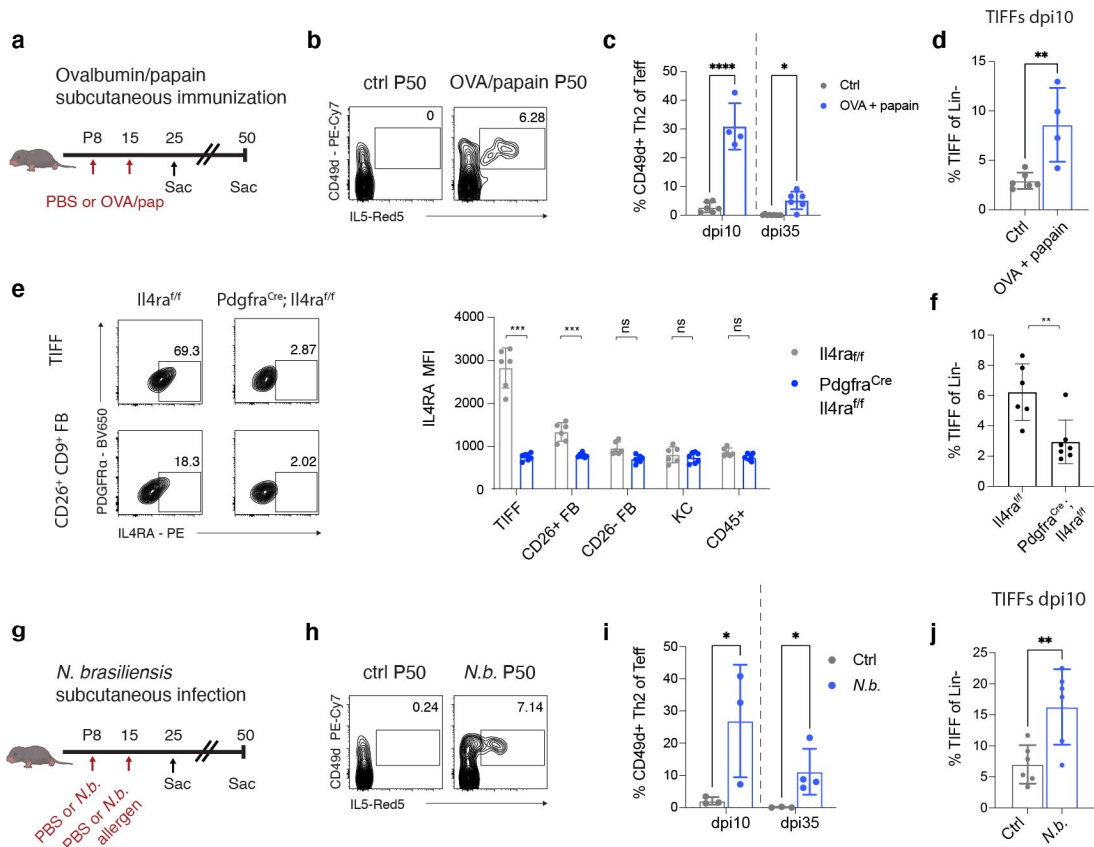


Figure S2.8- Th2-TIFF interactions and niche priming across multiple models of early life subcutaneous inflammation.

(a-d) Mice were immunized subcutaneously (s.c.) with ovalbumin (OVA) and papain. CD49d⁺ Th2 cells (b, c) and TIFFs (d) were quantified at indicated timepoints. $n=25$ animals I; 10 animals (d). **(e-f)** *Pdgfra^{Cre}; Il4ra^{fl/fl}* mice and Cre⁻ controls were injected with OVA-papain at P8 and P15. IL4RA expression (e) and TIFF frequency (f) were quantified at P25. $n=13$ mice. **(g-j)** Mice were infected s.c. with *Nippostrongylus brasiliensis* at P8 and boosted with s.c. *N. brasiliensis* allergen at P15. CD49d⁺ Th2 cells (g, i) and TIFFs (j) were quantified at indicated timepoints. $n=13$ mice (h); 12 mice (j). Data are displayed as mean +/- SD from one independent experiment; each experiment was reproduced 2-3 times. * $p < 0.05$, ** $p < 0.01$, *** $p < 0.001$ (all two-sided); Student's t-test (c-d, f, i-j); two-way ANOVA with Šídák multiple comparison test (e).

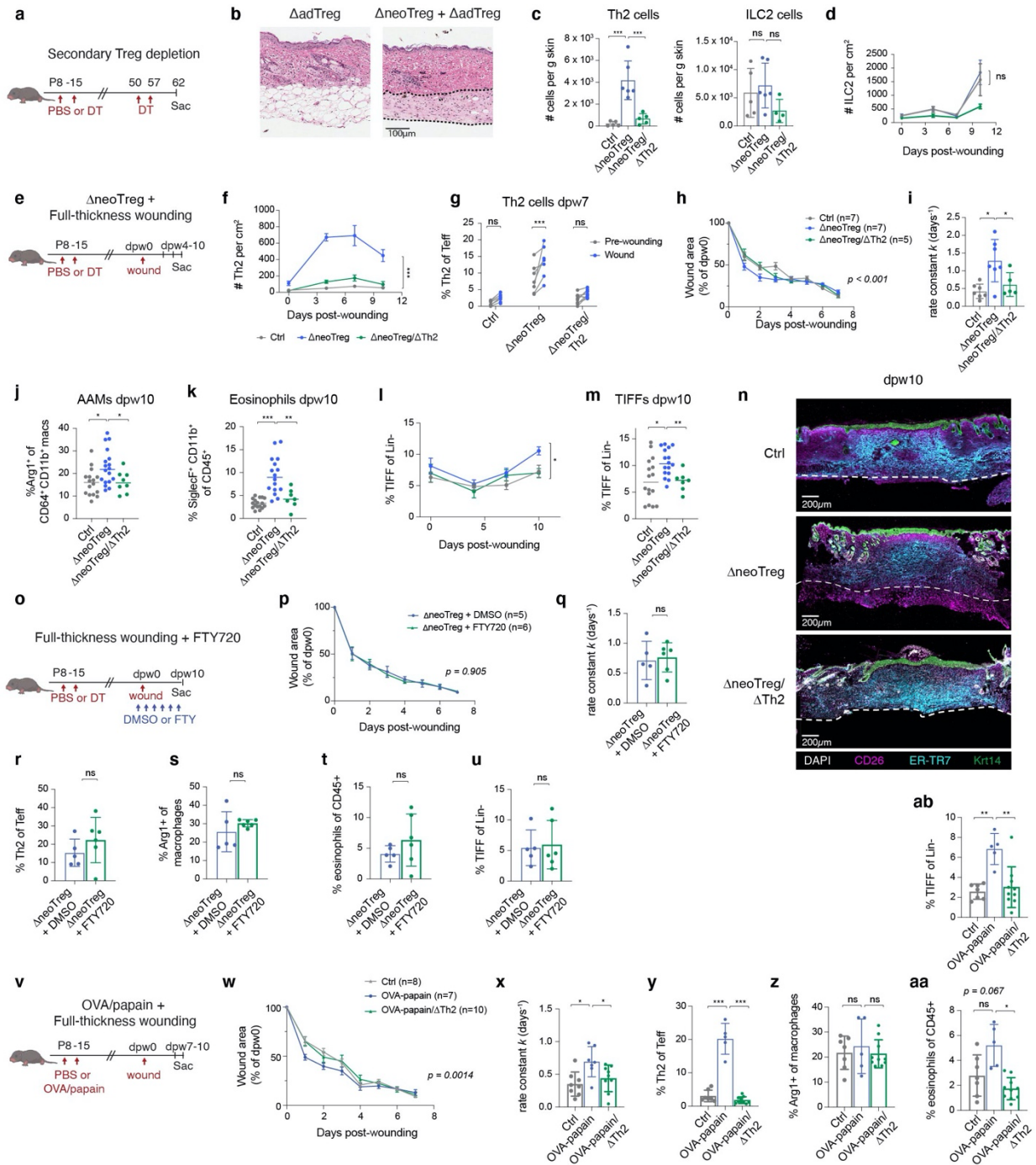


Figure S2.9- Neonatal Treg reduction primes skin for Th2-driven tissue reparative responses during adulthood. (a-b) Control and Δ neoTreg mice were aged to adulthood and then treated with two shots DT (identical to neonatal dosing regimen). Representative histology is shown with fibrous bands outlined. **(c)** Th2 and ILC2 cell numbers in adult ctrl (*Il5*^{Red5/+}; *FoxP3*^{DTR} + PBS), Δ neoTreg (*Il5*^{Red5/+}; *FoxP3*^{DTR} + DT), and Δ neoTreg/ Δ Th2 (*Il5*^{Red5/+}; *Rosa26*^{DTA/+}; *FoxP3*^{DTR}) mice. *n*=16 animals. **(d)** Wound bed ILC2 numbers (gated as CD45⁺ CD3⁻ CD4⁻ CD8⁻ Thy1⁺ IL5^{Red5+}). *n*=7-10 animals per data point in 2 pooled experiments per

time point (108 total). **(e-n)** Control, Δ neoTreg, and Δ neoTreg/ Δ Th2 mice were aged to adulthood and subjected to full-thickness cutaneous wounding. **(f)** Th2 numbers in skin 0 - 10 days post wounding (dpw). $n=4-11$ animals per data point in 2 pooled experiments per time point (89 total). **(g)** Th2 frequency in paired skin biopsies taken at dpw0 and dpw7. $n=22$ animals in one experiment. **(h-i)** Wound area was quantified daily, fit to a one-phase exponential decay model, and tested for equivalence of the rate constant (h). Rate constants of curves fit to each biological replicate are shown in (i). **(j-k)** Alternatively activated macrophage (AAM) and eosinophil frequency in dpw10 wounded skin. $n=42$ animals in 2 pooled experiments. **(l)** TIFF abundance in wound beds at 0 -10 dpw. $n=4-16$ animals in 2 pooled experiments (97 total). **(m-n)** Flow cytometric quantification (m) and IF microscopy (n) of CD26^{hi} TIFFs in wounds at dpw10. $n=39$ animals in 2 pooled experiments. **(o-u)** Δ neoTreg mice were aged to adulthood, wounded, and treated with FTY720 every other day. Wound closure (p-q) and flow cytometric quantifications of Th2 cells, alternatively activated macrophages (AAMs), eosinophils, and TIFFs are shown (r-u) are shown. $n=11$ animals. **(v-ab)** Neonatal mice were immunized with OVA/papain, aged to adulthood, and wounded. Wound closure (w-x) and flow cytometric quantifications of Th2 cells, alternatively activated macrophages (AAMs), eosinophils, and TIFFs are shown (y-ab). $n=22$ animals. Data are displayed as mean \pm SD (c-d, f, i-m, q-u, x-ab) or SEM (h, p, w). Results were reproduced over 2 independent experiments (a-d; o-ab) or 4 independent experiments pooled into two separate analyses (e-n). * $p < 0.05$, ** $p < 0.01$, *** $p < 0.001$ (all two-sided); ANOVA with Dunnett Multiple Comparisons Test (c, i-k, m, x-ab); least-squares quadratic regression with extra sum-of-squares F test (f, l); mixed-effects analysis with Šídák multiple comparison test (g); nonlinear one-phase exponential decay regression (h, p, w); Student's t-test (q-u) .

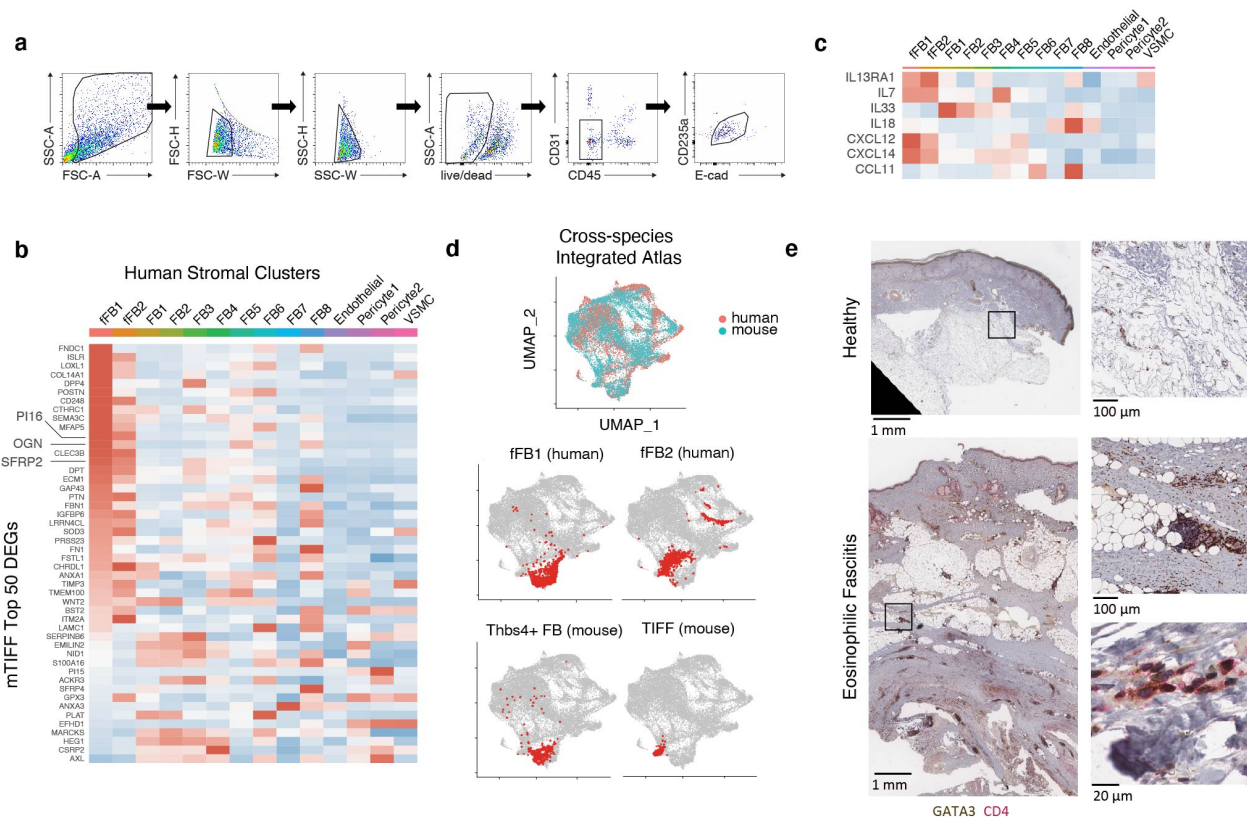


Figure S2.10- Characterization of human skin stroma.

(a) Gating strategy used to FACS-purify human Lin^- stromal cells ($CD45^- CD31^- Ecad^+$, $CD235a^+$). **(b)** Expression of top 50 murine TIFF (mTIFF) orthologs in human skin stroma, ranked by fold-change. **(c)** Expression of mouse TIFFs and Thbs4+ FB markers in healthy human stromal clusters. **(d)** Human and ortholog-converted mouse scRNAseq data were integrated and co-clustered. Cluster identities from single-species analyses (main fig. 2.4a-b) are shown projected onto the cross-species UMAP. **(e)** Sample histology of healthy and eosinophilic fasciitis lesional skin with IHC staining for GATA3 and CD4.

References

1. Al Nabhani, Z. & Eberl, G. Imprinting of the immune system by the microbiota early in life. *Mucosal Immunol.* **13**, 183–189 (2020).
2. Scharschmidt, T. C. *et al.* A Wave of Regulatory T Cells into Neonatal Skin Mediates Tolerance to Commensal Microbes. *Immunity* **43**, 1011–1021 (2015).
3. Scharschmidt, T. C. *et al.* Commensal Microbes and Hair Follicle Morphogenesis Coordinately Drive Treg Migration into Neonatal Skin. *Cell Host Microbe* **21**, 467-477.e5 (2017).
4. Kim, J. M., Rasmussen, J. P. & Rudensky, A. Y. Regulatory T cells prevent catastrophic autoimmunity throughout the lifespan of mice. *Nat. Immunol.* **8**, 191–197 (2007).
5. Nussbaum, J. C. *et al.* Type 2 innate lymphoid cells control eosinophil homeostasis. *Nature* **502**, 245–248 (2013).
6. Collins, N. *et al.* Skin CD4⁺memory T cells exhibit combined cluster-mediated retention and equilibration with the circulation. *Nat. Commun.* **7**, 11514 (2016).
7. Kobayashi, T. *et al.* Homeostatic Control of Sebaceous Glands by Innate Article Homeostatic Control of Sebaceous Glands by Innate Lymphoid Cells Regulates Commensal Bacteria Equilibrium. *Cell* **176**, 1–16 (2019).
8. Ali, N. *et al.* Regulatory T Cells in Skin Facilitate Epithelial Stem Cell Differentiation. *Cell* **169**, 1119-1129.e11 (2017).
9. Buechler, M. B. *et al.* Cross-tissue organization of the fibroblast lineage. *Nature* **593**, 575–9 (2021).
10. Joost, S. *et al.* The molecular anatomy of mouse skin during hair growth and rest. *Cell Stem Cell* **26**, 1–17 (2020).

11. Zhang, L. *et al.* Diet-induced obesity promotes infection by impairment of the innate antimicrobial defense function of dermal adipocyte progenitors. *Sci Transl Med* **5280**, (2021).
12. Driskell, R. R. *et al.* Distinct fibroblast lineages determine dermal architecture in skin development and repair. *Nature* **504**, 277–281 (2013).
13. Kimura-Ueki, M. *et al.* Hair cycle resting phase is regulated by cyclic epithelial FGF18 signaling. *J. Invest. Dermatol.* **132**, 1338–1345 (2012).
14. Kim, B. S. *et al.* TSLP Elicits IL-33-Independent Innate Lymphoid Cell Responses to Promote Skin Inflammation. *Sci. Transl Med* **5**, (2013).
15. Salimi, M. *et al.* A role for IL-25 and IL-33-driven type-2 innate lymphoid cells in atopic dermatitis. *J. Exp. Med.* **210**, 2939–2950 (2013).
16. Ricardo-Gonzalez, R. R. *et al.* Tissue signals imprint ILC2 identity with anticipatory function. *Nat. Immunol.* **19**, 1093–1099 (2018).
17. Obata-Ninomiya, K. *et al.* The skin is an important bulwark of acquired immunity against intestinal helminths. *J. Exp. Med.* **210**, 2583–2595 (2013).
18. Boothby, I. C., Cohen, J. N. & Rosenblum, M. D. Regulatory T cells in skin injury : At the crossroads of tolerance and tissue repair. *Sci Immunol* **5**, 1–13 (2020).
19. Correa-Gallegos, D. *et al.* Patch repair of deep wounds by mobilized fascia. *Nature* **576**, 287–292 (2019).
20. Naik, S. *et al.* Inflammatory memory sensitizes skin epithelial stem cells to tissue damage. *Nature* **550**, 475–480 (2017).
21. Findley, T. W., Chaitow, L. & Huijing, P. *Fascia: The Tensional Network of the Human Body.* (2013).

22. Stuart, T. *et al.* Comprehensive Integration of Single-Cell Data. *Cell* **177**, 1888-1902.e21 (2019).
23. Ramachandran, P. *et al.* Resolving the fibrotic niche of human liver cirrhosis at single-cell level. *Nature* **575**, 512–518 (2019).
24. Chan, K. K. *et al.* Eosinophilic Fasciitis Following Checkpoint Inhibitor Therapy: Four Cases and a Review of Literature. *Oncologist* **25**, 140–149 (2020).
25. Mortezaei, M., Barrett, M. & Edrissian, M. Successful treatment of refractory eosinophilic fasciitis with reslizumab. *JAAD Case Reports* **6**, 951–953 (2020).
26. Merrick, D. *et al.* Identification of a mesenchymal progenitor cell hierarchy in adipose tissue. *Science (80-.).* **364**, (2019).
27. Dahlgren, M. W. *et al.* Adventitial Stromal Cells Define Group 2 Innate Lymphoid Cell Tissue Niches. *Immunity* **50**, 1–16 (2019).
28. Spallanzani, R. G. *et al.* Distinct immunocyte-promoting and adipocyte-generating stromal components coordinate adipose tissue immune and metabolic tenors. *Sci. Immunol.* **4**, 1–14 (2019).
29. Schwalie, P. C. *et al.* A stromal cell population that inhibits adipogenesis in mammalian fat depots. *Nature* **559**, 103–108 (2018).
30. Scott, R. W., Arostegui, M., Schweitzer, R., Rossi, F. M. V. & Underhill, T. M. Hic1 Defines Quiescent Mesenchymal Progenitor Subpopulations with Distinct Functions and Fates in Skeletal Muscle Regeneration. *Cell Stem Cell* **25**, 797-813.e9 (2019).
31. Dahlgren, M. W. & Molofsky, A. B. Adventitial Cuffs: Regional Hubs for Tissue Immunity. *Trends Immunol.* **40**, 877–887 (2019).

32. Vainchtein, I. D. *et al.* Astrocyte-derived interleukin-33 promotes microglial synapse engulfment and neural circuit development. *Science* (80-.). **359**, 1269–1273 (2018).
33. Hagan, A. S., Zhang, B. & Ornitz, D. M. Identification of a FGF18-expressing alveolar myofibroblast that is developmentally cleared during alveologenesis. *Dev.* **147**, (2020).
34. Camberis, M. *et al.* Evaluating the in vivo Th2 priming potential among common allergens. *J. Immunol. Methods* **394**, 62–72 (2013).
35. Bankhead, P. *et al.* QuPath: Open source software for digital pathology image analysis. *Sci. Rep.* **7**, 1–7 (2017).
36. Yang, B. *et al.* Single-Cell Phenotyping within Transparent Intact Tissue through Whole-Body Clearing. *Cell* **158**, 945–958 (2014).

Publishing Agreement

It is the policy of the University to encourage open access and broad distribution of all theses, dissertations, and manuscripts. The Graduate Division will facilitate the distribution of UCSF theses, dissertations, and manuscripts to the UCSF Library for open access and distribution. UCSF will make such theses, dissertations, and manuscripts accessible to the public and will take reasonable steps to preserve these works in perpetuity.

I hereby grant the non-exclusive, perpetual right to The Regents of the University of California to reproduce, publicly display, distribute, preserve, and publish copies of my thesis, dissertation, or manuscript in any form or media, now existing or later derived, including access online for teaching, research, and public service purposes.

DocuSigned by:

Ian Boothby

B0EB23A4DC58418...

Author Signature

11/28/2021

Date